BEILSTEIN JOURNAL OF NANOTECHNOLOGY

Correlative approaches in materials science – from the micrometer to the nanometer scale

Edited by Matthias Mail and Christian Kübel

Imprint

Beilstein Journal of Nanotechnology
www.bjnano.org
ISSN 2190-4286
Email: journals-support@beilstein-institut.de

The *Beilstein Journal of Nanotechnology* is published by the Beilstein-Institut zur Förderung der Chemischen Wissenschaften.

Beilstein-Institut zur Förderung der Chemischen Wissenschaften
Trakehner Straße 7–9
60487 Frankfurt am Main
Germany
www.beilstein-institut.de

BEILSTEIN JOURNAL OF NANOTECHNOLOGY

Characterisation of a micrometer-scale active plasmonic element by means of complementary computational and experimental methods

Ciarán Barron, Giulia Di Fazio, Samuel Kenny, Silas O'Toole, Robin O'Reilly and Dominic Zerulla*

Full Research Paper

Open Access

Address:
School of Physics, University College Dublin, Belfield, Dublin 4, Ireland

Email:
Dominic Zerulla* - dominic.zerulla@ucd.ie

* Corresponding author

Keywords:
active plasmonics; atomic force microscope; scanning Joule expansion microscopy (SJEM); surface plasmon polariton

Beilstein J. Nanotechnol. **2023,** *14,* 110–122.
https://doi.org/10.3762/bjnano.14.12

Received: 31 July 2022
Accepted: 27 December 2022
Published: 16 January 2023

This article is part of the thematic issue "Correlative approaches in materials science – from the micrometer to the nanometer scale".

Guest Editor: M. Mail

Abstract

In this article, we investigate an active plasmonic element which will act as the key building block for future photonic devices. This element operates by modulating optical constants in a localised fashion, thereby providing an external control over the strength of the electromagnetic near field above the element as well as its far-field response. A dual experimental approach is employed in tandem with computational methods to characterise the response of this system. First, an enhanced surface plasmon resonance experiment in a classical Kretschmann configuration is used to measure the changes in the reflectivity induced by an alternating electric current. A lock-in amplifier is used to extract the dynamic changes in the far-field reflectivity resulting from Joule heating. A clear modulation of the materials' optical constants can be inferred from the changed reflectivity, which is highly sensitive and dependent on the input current. The changed electrical permittivity of the active element is due to Joule heating. Second, the resulting expansion of the metallic element is measured using scanning Joule expansion microscopy. The localised temperature distribution, and hence information about the localisation of the modulation of the optical constants of the system, can be extracted using this technique. Both optical and thermal data are used to inform detailed finite element method simulations for verification and to predict system responses allowing for enhanced design choices to maximise modulation depth and localisation.

Introduction

Active plasmonics has been gaining attention from the research community for its role in the development of photonic devices [1,2], low-loss waveguides [3], and imaging systems [4]. It is an emerging subfield of plasmonics, which focuses on controlling electromagnetic fields at the nanoscale through external manipulation of the materials' properties. Here, we present the charac-

terisation of a recently developed active plasmonic element [5] through two complementary experimental methods. Active plasmonic elements have applications in future imaging technologies and as modulators in optoelectronic couplers for photonic circuits. Finite element method (FEM) simulations are used to validate both experimental approaches, allowing for cross-verification of results and giving greater insight into the underlying physical phenomena.

Surface plasmon polaritons (SPPs) are mixed states of photons and electron density waves propagating along the interface between a conductor and a dielectric. As a result of this phenomenon, an electric field strongly confined in the *z*-direction is produced at the interface. As direct excitation of a smooth metallic surface does not form SPPs, certain configurations have been developed to provide the conditions allowing for its formation. These were initially proposed by Otto [6] and Kretschmann and Raether [7]. To meet momentum-matching conditions necessary for the formation of SPPs, such configurations rely on the presence of an optically denser dielectric material with which the light interacts before reaching the metal. Light–matter interactions which give rise to the formation of SPPs can be classified into a sub-field of photonics known as plasmonics [8]. Investigations into SPPs provide vital insights into fundamental physical phenomena at the nano- and mesoscales [9-15], as well as more practical applications in Raman spectroscopy in the form of surface-enhanced Raman spectroscopy (SERS) [16] and other spectroscopic techniques [17,18]. SPPs also find uses in fields such as ultrasensitive detection methods [19,20], as their formation is highly dependent on refractive index changes, and sub-wavelength optics [21]. Our active plasmonic element also provides the potential for an even more sensitive technique. Active plasmonics has further advantages due to the tunable nature of the physics underneath and its ability to interact with electronic circuits [22].

The performance of the active element can be characterised in terms of modulation localisation and depth. Localisation addresses how confined the active control is at the nanoscale, while modulation depth is an indicator of how well the external manipulation changes the properties of the device. Characterisation of both localised temperature distribution and optical constants plays a key role for further applications and is required to optimise the operation parameters for the active plasmonic element.

Previous studies [23,24] investigated the effects of gap size using a fine tunable mechanical separation as a means to control the intensity of a travelling SPP on silver. In contrast, in the present work, the modulation of the device's response is obtained through changes in the optical constants via electrical signals. It is well understood that heating affects the electrical permittivity of metals [25-28] and dielectrics [29,30]. This, in conjunction with Joule heating, is used to generate the desired effects.

The active plasmonic element proposed (Figure 1) consists of a nano- or mesoscale constriction in a 48 nm thick layer of silver. Applying a current through the silver layer results in increased heating at the constriction due to the reduced cross section. Consequently, given the dependence of the materials electric permittivity on temperature, the optical response will change locally.

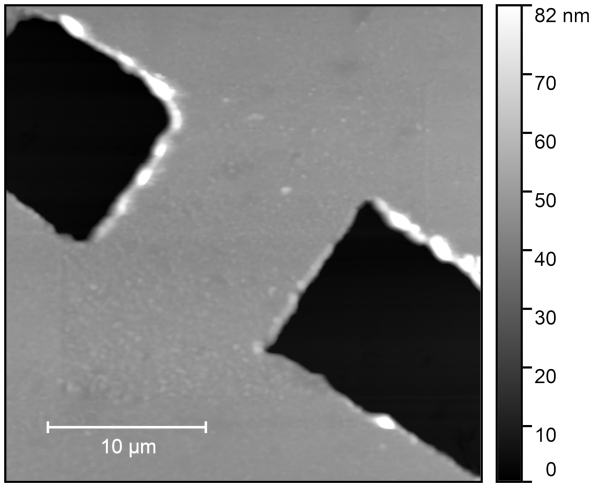

Figure 1: An AFM image of a 10 × 10 µm^2 constriction in a 48 nm thin silver film on a sapphire substrate. The total area of the AFM image is 30 × 30 µm^2. Two cuts (black channels) split the silver layer (grey) into two parts, connected only by the bridge depicted in the image. Under the application of a current, the metal heats up due to the Joule effect. The presence of a constriction in the metal (the bridge) results in a localised heating effect.

In this work, we have adapted two unconventional correlative methods to investigate the system exploiting their ability to directly probe the parameters of interest. The first method is based on an attenuated total reflection (ATR) setup whose versatility is enhanced through the addition of a lock-in amplifier (LIA) investigating the changes in the reflectivity induced by a modulated electric current. The acquisition of a surface plasmon resonance (SPR) curve is a common method to characterise a plasmonic far-field response [31] which is highly sensitive to small changes in the refractive index of the metal and dielectric. Because of this extreme sensitivity, small changes in the local temperature, and hence in optical constants, will result in subtle but appreciable changes of reflectivity in the SPR curve. Homodyne detection, with the modulated electric currents as reference, enables a detailed examination of the

microscale active plasmonic element. Temperature changes are induced by the applied current through the microoptical element. Analysis of both the lock-in signal and the classical SPR curve from angular interrogation enables the deduction of the complex optical constants. Furthermore, the presence of strong peaks indicates the ability to maximise the modulation of the element's optical response. While the classical SPR response integrates over the whole illuminated area, the LIA curve extracts the changes in reflectivity localised to the active element. This leads to a modulated local near field, which has applications in the development of new imaging technologies using this localised field to go beyond the diffraction limit of light. Because the temperature is geometry-dependent in the constriction, it is necessary to map the thermal distribution in the vicinity of the element. The experimental complementary method therefore investigates the thermal response of this active plasmonic element at a high spatial resolution. Knowledge of the distribution leads to predictions on how the near field will be locally affected, which is key for understanding the behaviour of the active plasmonic element. The heating distribution is investigated by means of scanning Joule expansion microscopy (SJEM) [32]. The technique provides a method to obtain the relative temperature distribution at the nanoscale starting from the measurement of induced thermal expansion, which can be directly mapped in a standard AFM-based image using a LIA. This also provides great insight into nanomechanical thermal interactions.

Knowledge of both physical parameters, the optical response, and heating allows cross-verification and understanding of the underlying mechanisms causing changes in the active plasmonic element. The FEM simulation software COMSOL Multiphysics has been used to predict and confirm the dynamic temperature distribution and the optical response of the system.

Experimental

The manufacturing of the active plasmonic elements employed in the present work is detailed in [5]. At first, a 48 ± 2 nm film of silver is deposited on a sapphire substrate via physical vapour deposition (PVD). After this, two separate AFMs are used to machine channels in the silver film to create the desired constriction, which in this case measures 10 µm. The tip of the AFM is held at a set loading force in contact with the thin metal film and moved to remove the silver.

The investigations carried out consist of two experimental correlative methods. The first method is the above discussed enhanced SPR experiment, based on an ATR setup whose sensitivity is enhanced through the addition of a lock-in amplifier. The second method probes the temperature distribution surrounding the active element through SJEM mapping the thermal expansion of the metallic surface using an AFM. Both methods are further reinforced through the use of three-dimensional simulations. A description of the experimental methods of both investigations is detailed below as well as the FEM parameters used to simulate the behaviour of an active plasmonic element.

Enhanced SPR experiment

For angular interrogation of the plasmonic response of the active plasmonic element, an enhanced SPR experiment (Figure 2) was used. The system under investigation consists of

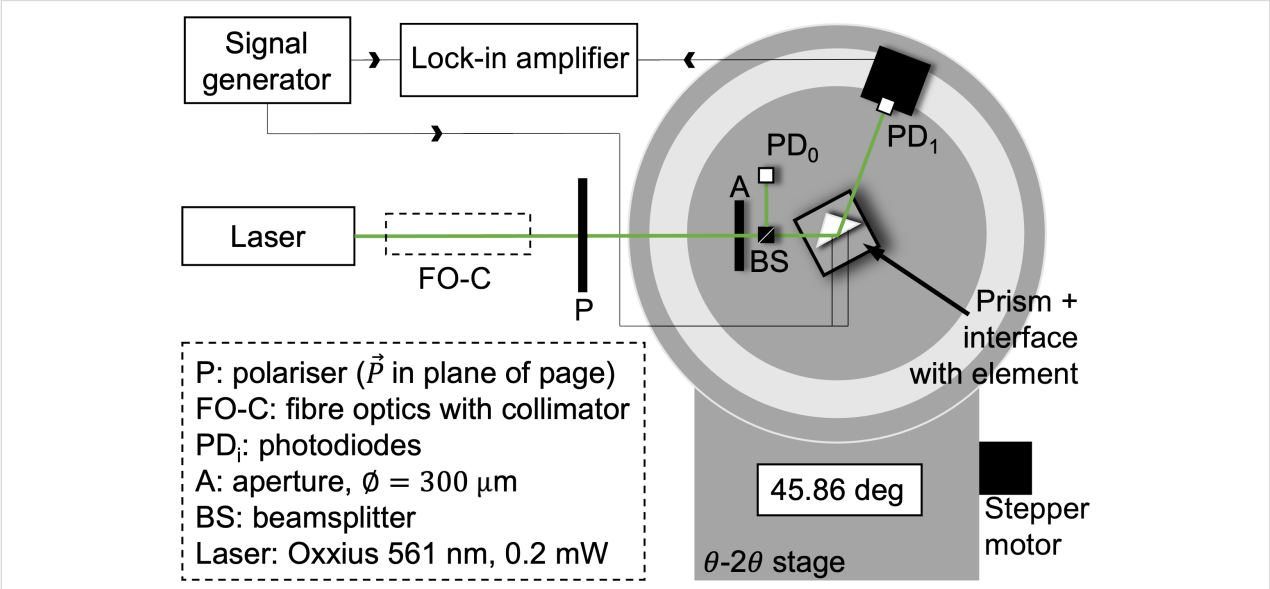

Figure 2: A schematic of the enhanced SPR experiment.

a constriction in the silver film such that a current modulated at a particular frequency affects its optical properties via Joule heating. The signal is acquired by a photodiode and further processed by a lock-in amplifier (Ametek 5210), with the driving signal of the modulated voltage acting as reference. The DC component of the light results in a typical SPR curve while the modulated signal from the lock-in amplifier produces a more sensitive signal. This yields the variation in the optical constants as a function of the thermal modulation of the active element.

An Oxxius single-frequency CW laser at 561.4 nm, typically incident at 0.2 mW after filtering, was used as the incident light source. The collimated light from an optical fibre was spatially filtered through a 300 μm aperture and a polariser aligned to the plane of rotation ensuring *p*-polarisation for SPP excitation as seen in Figure 2. The reference light is recorded after the aperture and reflected from a cube beam splitter, with the signal photodiode placed on the 2θ arm of a high-accuracy (18 arcsec resolution) Siemens θ–2θ X-ray diffractometer stage with inbuilt goniometer to collect light reflected from the interface. The absolute angular position is manually determined by aligning multiple back reflections, with an estimated error of approximately 4.5 arcmin. The stage's gearing is driven by a high-current pure sine signal such that motor steps cannot be missed, thus eliminating this as a source of error. The Kretschmann configuration was placed horizontally at the centre of the stage rotating at θ. This configuration consists of a fused silica prism with a sapphire slide optically coupled using refractive index matching oil (n = 1.516). This configuration was also used in the simulations. A sapphire slide was used as the deposition substrate for a thin silver film of 48 nm. The incident angles were referenced to the air–prism interface. The sinusoidal current was generated using a function generator with a current buffer to ensure impedance matching to the system under investigation. A transimpedance-amplified photodiode signal with active DC and high-frequency filtering was fed to the lock-in amplifier, while the non-filtered signal was recorded for the SPR reflected signal. The modulated voltage applied was of the same form as the simulations with frequency f = 631 Hz and offset such that the resultant signal was entirely positive.

At each angular position, the signals from the photodiodes were continuously recorded for one time constant following an adequate rest period, after which the in-phase components of the lock-in amplifier (X-components) were recorded using an Arduino-controlled analog-to-digital converter. The reference phase of the LIA was chosen to maximise X. The LIA was set to a time constant of τ = 300 ms, with second-order low-pass filtering and a sensitivity of 30 mV to avoid spurious input overloads. Once this set was recorded, the stage was moved 1×10^{-2} degrees to the next angular position in the scan. The substrate used to generate the SPR response is sapphire with a refractive index of n = 1.7717 at λ = 561 nm.

SJEM experiment

To further characterise the active plasmonic element, in complement with the SPR curve measurements above, the thermal distribution due to Joule heating of the active element was measured through the use of scanning Joule expansion microscopy. The application of a current to the metallic element results in Joule heating. As stated previously, this heating results in an appreciable change in the optical constants of the silver enabling modulation of its plasmonic response. This heating also results in thermal expansion of the element. This expansion will result in deflection of an AFM cantilever scanning the surface. If a sinusoidal voltage is applied to an electrically conducting sample, such as the active plasmonic element discussed here, the resulting thermal expansion will be periodically modulated at the frequency of the applied voltage. When an AFM scan is performed on an element which is periodically modulated, the expanded surface will also be captured by the AFM. A lock-in amplifier can then be used to extract the periodically occurring expansion of the topography from a surface scan performed while the element is modulated at a known frequency. This is the basis for SJEM measurements.

Here, SJEM measurements have been performed using an Oxford instruments Cypher-S AFM and a signal recovery 7270 DSP lock-in amplifier. Figure 3 illustrates the setup used to perform such measurements. An Adama NM-RC probe (spring constant: 290.3 N/m, nominal resonance frequency: 814 kHz) has been used in contact mode to scan the topography of an electrically modulated sample with a loading force of 1.9 μN. This particular probe is intended for use in nanomechanical operations such as lithography and machining. The high spring constant of this cantilever has the advantage of minimising the unwanted deflection of the cantilever resulting from electrostatic interaction of the potential on the surface and the probe. The tip is constructed from wear-resistant diamond with a tip radius of 10 ± 5 nm. The deflection sensitivity of the probe was measured to be 81.09 nm/V.

To perform an SJEM measurement, a sinusoidal voltage is applied to the metallic element. The surface of the element is then scanned with an AFM in contact mode. Contact mode was selected in this case to ensure the probe captured the deflection due to thermal expansion while minimising artifacts caused by the periodic potential on the surface. The sample was driven with a frequency of 1227 Hz, well below the 170 kHz limitation on the response time of the z-piezo control of the scanner in

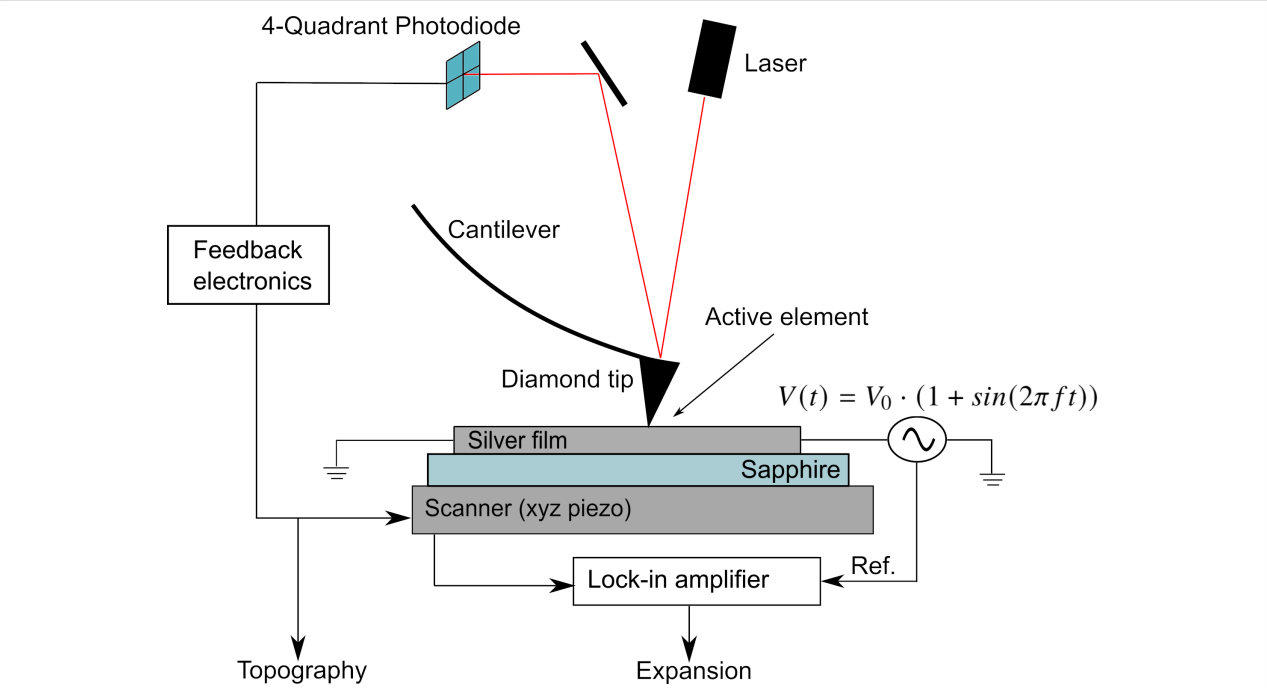

Figure 3: Schematic describing the experimental setup used to perform SJEM measurements on a modulated element.

the Cypher AFM. This frequency is also well below the resonance frequency of the selected cantilever avoiding unwanted resonant oscillations in the cantilever as a result of the periodic force applied by the expanding surface when deflecting the cantilever. In principle, the drive frequency of the active element could be the same for both experiments. However, the higher frequency provided an increased number of heating cycles over which to integrate given the chosen scan parameters listed below. Ideally, the active element would be modulated in the same fashion in both experiments. However, the information extracted in both cases does not depend on the drive frequency, given the thermal relaxation time of such a metallic element on a sapphire substrate is of the order of nanoseconds, and as such there is no need for matching drive frequencies. AFM scans were performed on a 30 × 30 μm^2 window with a setting of 512 points per line. The resulting pixel size is 58.7 nm. AFM scans were then performed at a scan rate of 0.1 Hz resulting in the tip being over each pixel of the image for approximately 10 ms. At a drive frequency of 1227 Hz, this corresponds to more than ten cycles of expansion and contraction per point for the lock-in amplifier to integrate over. The time constant for the lock-in process was set to 10 ms to match the time the tip is over each pixel. The sensitivity of the LIA was set to 200 µV. The applied voltage was set based on the current density through the sample so as to match the conditions in the above SPR measurements as closely as possible. The Cypher-S AFM is capable of detecting dynamic changes in height of the sample down to the sub-picometer scale. Scans were performed at multiple current densities to demonstrate the differences in temperature distribution surrounding the sample as a function of applied current. For higher current densities, a wider distribution of the temperature is expected. A current buffer was used to ensure the current density through the element was consistent throughout an AFM scan. The probe was left electrically floating during scanning. While leaving the probe floating is counterproductive from the perspective of minimising electrostatic interaction, the possibility of current flow through the tip to ground is eliminated. As with the LIA phase selection for the SPR measurements discussed above, the phase was selected so as to maximise the *X*-component of the LIA signal. SJEM measurements were performed for current densities of 45, 48.2, 51.8, 54, and 58 mA/μm^2, the results of which can be found below.

Simulations

Finite element analysis simulations using COMSOL Multiphysics 6.0 were employed to cross-verify the results obtained from both methods. The schematic in Figure 4 illustrates the steps involved in performing such simulations.

Initially, a model of the silver structure described above was built on top of a sapphire substrate. This model is a representative subsection of the substrate and silver film on which the physical active element was fabricated. The thermal behaviour of the element was simulated for an applied alternating electrical potential with a DC offset through the thin silver layer

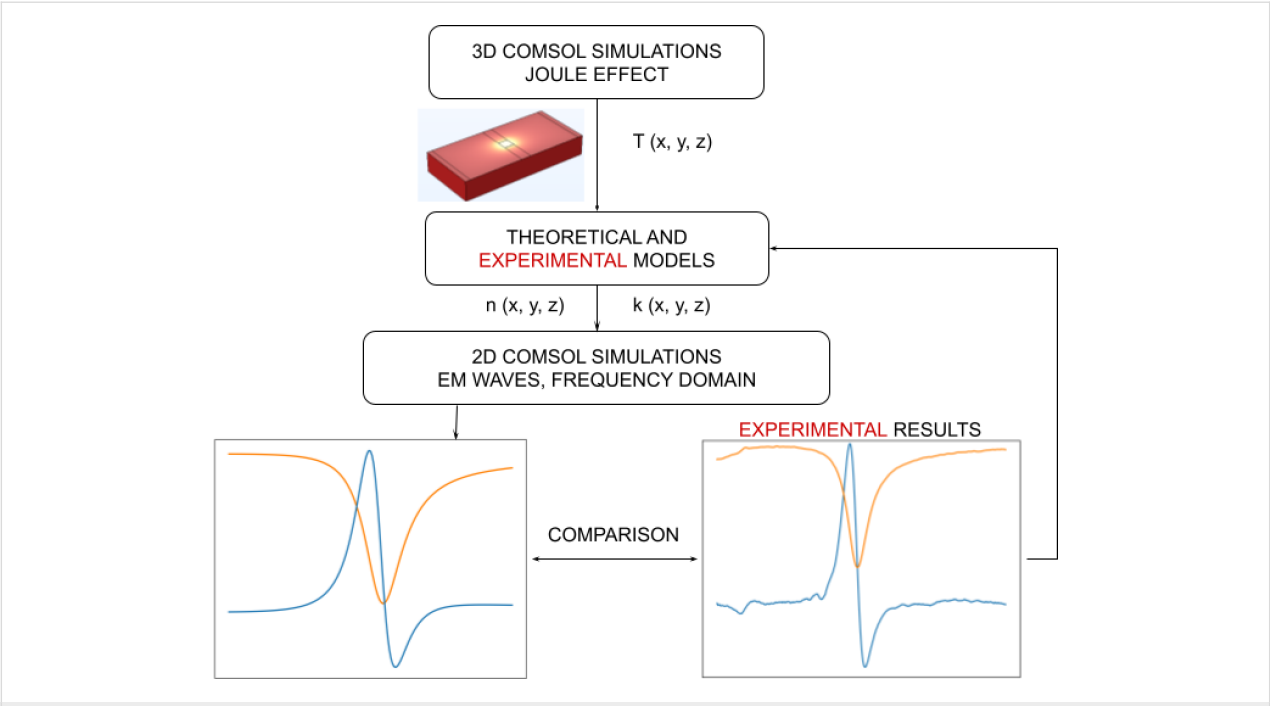

Figure 4: Flow diagram of simulation process.

and compared to experimental findings. A temperature boundary condition was imposed on both the bottom and lateral surfaces of the model, keeping them at room temperature (293.15 K).

An alternating voltage with a DC offset $V_{in}(t) = V_0 \cdot (1 + \sin(2\pi ft))$, where V_0 = 200.0 mV and f = 631 Hz, was applied across the silver layer. The voltage was chosen so as to guarantee a correspondence with the experiments in terms of current density. The application of a voltage with an AC component resulted in a spatial temperature distribution changing periodically as a function of the time. The temperature distribution shown in the Results section below in Figure 12 refers to the point in time t = 1.68 ms. Results in terms of temperature distribution were therefore used to cross-verify the experimental findings coming from the SJEM experiment.

The second part of the computational work focused on the changes induced by the temperature on the optical properties of the system under analysis. Such changes lead to differences in the reflectivity curve acquired by means of the enhanced SPR experiment. In order to back up the experimental findings, electromagnetic simulations were performed both in a cold state, using room temperature refractive indices, and in a hot state. Johnson and Christy [33] electrical permittivity values were used to model the silver layer at room temperature. The electromagnetic simulations of the heated system were performed starting from a temperature distribution extracted from the thermal simulations previously performed (t = 1.68 ms). This means that a temperature value is associated to each spatial point. Starting from two tables, one for sapphire and one for silver, containing spatial coordinates and corresponding temperature values, the data illustrated in Winsemius et al. [27] were used to model the influence of temperature on the silver's permittivity while for sapphire results from Thomas et al. [34] were employed. The resulting tables, again one for each material, containing the spatial points and refractive indices were subsequently imported into COMSOL to define the heated materials. All values were evaluated at the selected operational wavelength λ = 561 nm. For reference, in the following Table 1, we

Table 1: Refractive indices for silver and sapphire at room temperature and at the highest temperature reached by the structure at time t = 1.68 ms.

	Sapphire		Silver	
temperature (K)	293.15	338.26	293.15	340.00
n	1.7697	1.7703	0.056299	0.060110
κ	0.0	0.0	3.6867	3.6868

report the refractive index values for both sapphire and silver at room temperature and at the highest temperature reached by the simulated structure. The refractive index of air was taken as $n_{air} = 1.00$.

The optical response of the sapphire–metal–air structure was quantified in terms of reflectivity at different incoming excitation angles, computed by means of COMSOL optical simulations. A two-dimensional simulation space was set up in COMSOL, and the electromagnetic waves in the frequency domain module were used to set up the problem (see Figure 5). The input port was set to simulate an incoming TM wave, and Floquet periodic conditions were imposed on the side boundaries. A perfectly matched layer (PML) was added on top of the air layer in order to avoid back reflection. Total reflectivity data were collected at the output port.

Integrating this simulation setup with the temperature distribution output from the previous step allows for an accurate representation of temperature-dependent changes on the reflectivity curve. This produces a representation of the modulation depth which is seen when looking at the difference of hot and cold states using a lock-in amplifier.

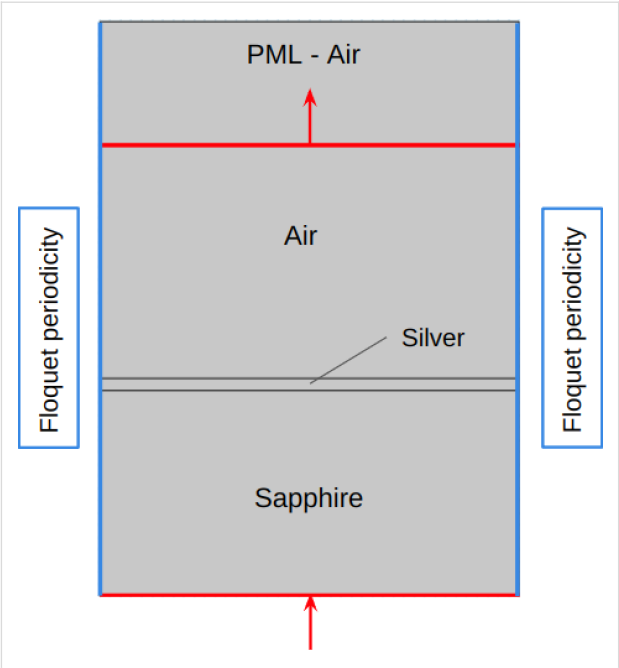

Figure 5: FEM optical simulation setup.

Results

First, the results of the SPR curve with the lock-in amplifier which measures the difference between a heated and room temperature constriction are presented. Subsequently, the results obtained from SJEM measurements are analysed. Finally, both experimental results are compared with simulations.

Enhanced SPR experiment

Figure 6 shows the experimental data and simulated SPR curves. It is clear that all expected main features of the curves

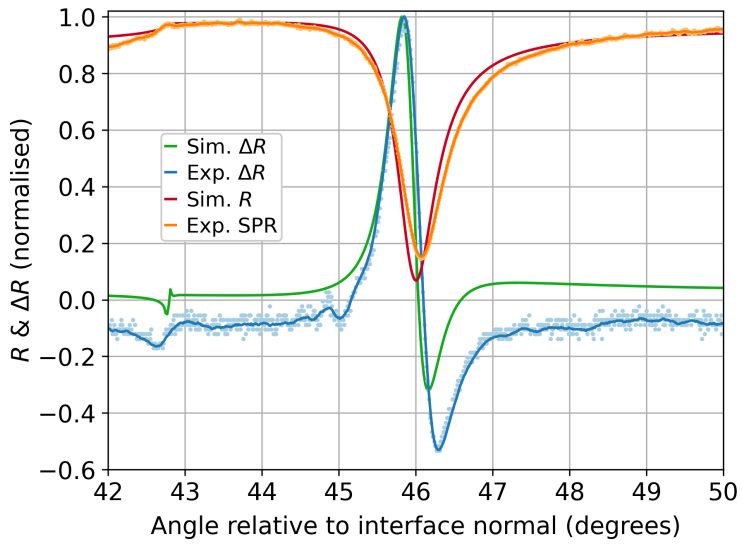

Figure 6: Plots of the enhanced SPR curves for a sapphire–silver–air configuration excited at 561 nm showing the typical shape in red and orange, and Δ*R* response, taken from the lock-in amplifier (*X*) component, or the effective difference between the coldest and hottest states in blue and green for a modulated 20 μm square active element. Orange shows the experimental curve normalised to the simulation maximum for an applied (RMS) current density of 71 mA/μm^2. The angular position of the TIR response of the experimental SPR curves has been calibrated to the simulation. The solid lines are a centred moving average for each experimental curve. Experimental errors are considered below in Figure 8. The results of COMSOL 2D optical simulations were computed for a system at room temperature and with a temperature distribution extracted from thermal simulations. The curves presented are the average between those two states (red) and their difference (green).

are present for both approaches. The SPP angle corresponds to a minimum in reflection and, in this case, was 46.07°. The results show a critical total internal reflection (TIR) angle at approximately 42.7° from the surface normal. Both results are in line with theoretical predictions for the employed substrate.

While the experimental measurements are exploiting a continuous sinusoidal modulation which oscillates between two states (i.e., hot and cold), the simulations are comparing only these extreme states. The simulation was performed on sapphire and silver at room temperature and at the heated state. In the experiment, the resulting SPR curve, recorded in parallel to the extracted lock-in curve, is effectively a weighted average of all temperature states. Therefore, the simulated SPR curves obtained from both the cold and the heated structure were averaged to obtain the red curve in Figure 6, and their relative difference was taken to generate the green curve.

The slight discrepancy between the minimum in the measured SPR curve (orange) and the theoretical version (red) is assumed to be ascribable to the data set used to model the simulated materials. To describe silver's optical constants at room temperature, Johnson and Christy [33] data were employed, but the refractive index of the silver material used in the experiments differs slightly. The measured SPR curve is slightly broader than the simulated one. This is due to experimental broadening (in particular, the divergence of the laser beam), surface roughness, and further temperature-induced degradation effects that are not taken into account in the simplified simulation setup employed.

In order to determine the quality of the agreement between simulations and experimental data, we additionally carried out a comparative study between two electromagnetic simulations. Both simulations were set up at room temperature (293.15 K, cold state) and using the same substrate, but the silver layer was characterised in two different ways, using two of the most cited sources in the field. At first, the refractive index was defined using Johnson and Christy dataset [33]. Subsequently, the same simulation was repeated exploiting data from Wu and co-workers [35]. The result in terms of SPR curve is plotted in Figure 7.

Directly comparing the simulated and experimental plasmonic resonance positions between the SPR curves in Figure 6, there is a difference of 0.07° in the position of the plasmonic dip. While this is outside the estimated error accumulation of approximately 0.02° on the experimental data, the two simulations show a discrepancy of 0.14°. This clearly shows that the shift measured between the experimental SPR curve and the simulated one can be brought back to the difference between literature data for refractive indices and the optical properties of the film.

On close inspection of Figure 6, in contrast to simulations, the experimental measurements reveal additional peaks on the leading edge of the main peak about 45.0°. Detailed analyses reveal this is due to ageing of the silver and surface modifications. There are others at about 45.5°, which, altogether, will be discussed in a subsequent paper. At this stage, experiments with active elements of different sizes reveal that the ratio between heated and non-heated surface illuminated by the laser beam

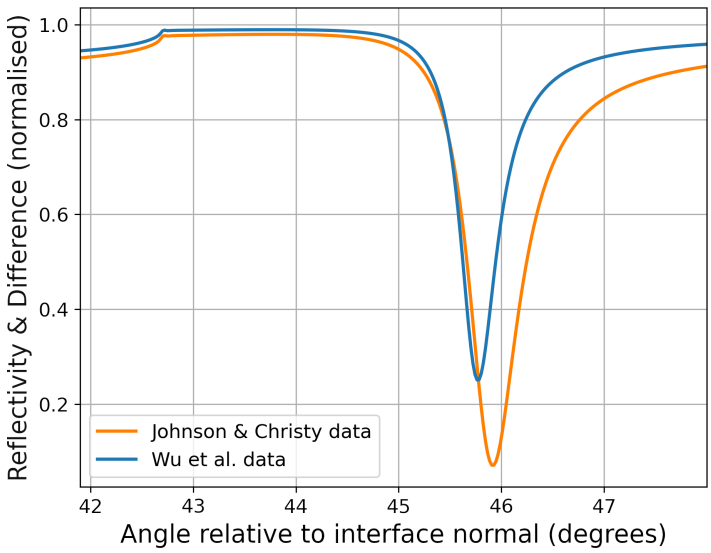

Figure 7: SPR curves resulting from electromagnetic simulations performed on a similar structure at room temperature. Different data sets were employed to model the silver layer. There is a noticeable shift in the position of the minimum of the two curves.

influences the intensity of this effect. The ability to observe these details demonstrates the high sensitivity of this technique to the differences in optical constants of small areas under investigation. This effect, while highly interesting, deserves its own dedicated investigation and, hence, falls outside the scope of this paper.

In Figure 8, the response of both the typical SPR curve and the LIA signal at four selected current densities and, hence, varied temperature, are shown. Current densities of 71–143 ± 1 mA/μm^2 in steps of ≈24 mA/μm^2 were used for a 20 μm square element. While not identical to the SJEM experimental current densities, we ensure that they are of similar magnitude, 45–58 ± 1 mA/μm^2, hence, enabling comparison between the experiments. The increasing temperature is seen through the typical SPR curves as a broadening in the plasmonic dip and shift of the minimum angle towards higher angles, as expected.

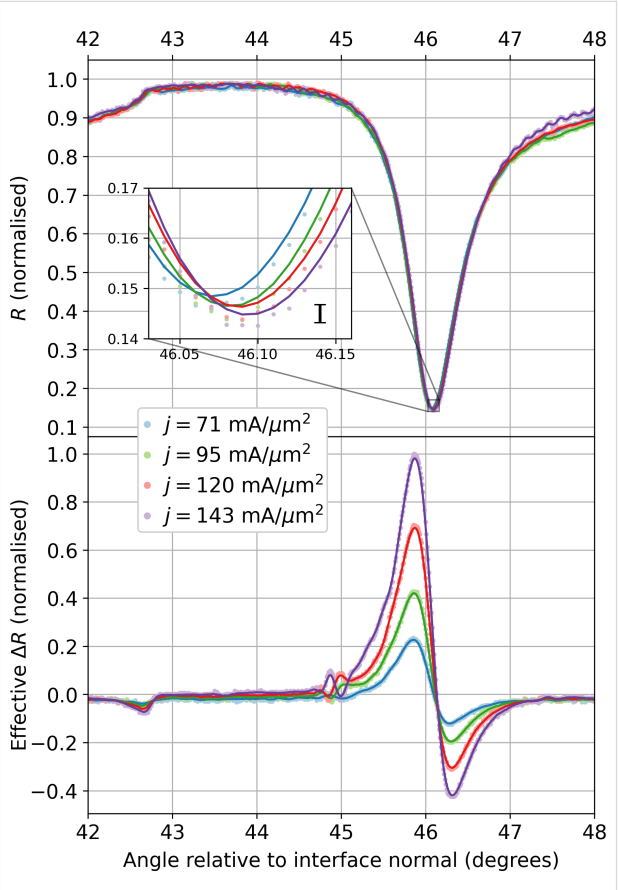

Figure 8: Plots of the enhanced SPR curves showing the typical SPR curve shapes (top) for a sapphire–silver–air configuration excited at 561 nm and the effective change in reflectivity (bottom) for a 20 μm square active element modulated with an applied (RMS) current density of 71–143 mA/μm^2 in steps of ≈24 mA/μm^2. The lock-in signal error is estimated at 0.5%. The inset emphasises the shift in the plasmonic resonance position for increasing temperatures with the error of the SPR signals included in black. The current densities were applied in ascending order. The solid lines are a centred moving average for each curve.

Experimentally, the SPR curve is measured directly by the photodiode. The modulation depth of the reflected light selected here, in this simple geometry, is of the order of 1% with respect to the total light intensity. To improve the signal-to-noise ratio, a lock-in amplifier is used to detect modulated signals referenced at the driving frequency. The aforementioned SPR characteristics manifest in the *X*-component signal of the lock-in amplifier, which originates from the changes in the temperature and is highly sensitive to a modification of the systems morphology with a fixed phase relationship.

As the temperature is modulated, these alterations occur in tandem with the driving frequency. The increased temperature affects a change in the optical constants of the system, thereby altering the SPR curve including its resonance position. The difference is measured directly with the driving signal as reference using a lock-in amplifier. This in-phase signal of the LIA is a direct measurement of the changes in the SPR curve.

In conclusion, both the ATR response and its characteristic plasmonic dip in reflectivity are present in the simulated curve and their angular position show a very good agreement with experimental results. The relative difference between the two curves behaves in line with the observed lock-in signal, as reported in Figure 6, validating the measurements.

SJEM experiment

Figure 9 shows an AFM image of the silver surface in a 30 × 30 μm^2 window centered on the active element. On the left is a topographical image of the surface showing the element, which consists of a constriction of approximately 10 × 10 μm^2 in the silver film. The accompanying colour bar denotes the height of the sample in reference to the sapphire substrate below. The dark regions are areas where the silver has been removed as described above. On the right is an SJEM measurement showing the thermal distribution around the active element by mapping the thermal expansion of the silver element for each pixel of the image. The SJEM image shows the largest expansion occurring at the centre of the element, decreasing away from the centre of the element approximating a Voigt function. The associated colour bar shows the highest expansion as lighter coloured regions and areas of lower expansion as darker regions. The expansion around the element is representative of the temperature distribution in the heated state of modulation and appears to follow the expected spread.

Figure 10 shows a Voigt function fit to a profile along the centre of the expansion image seen in Figure 9. The measured

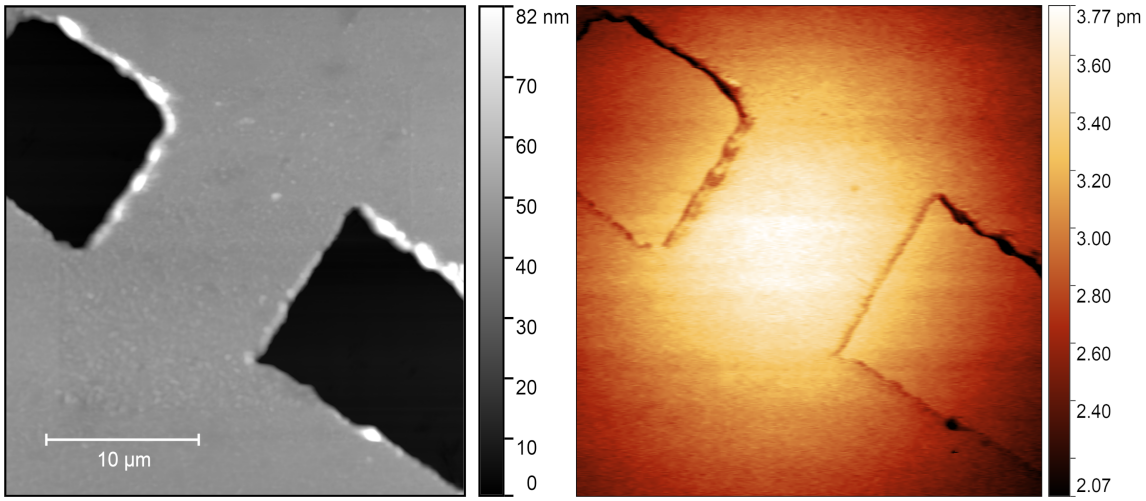

Figure 9: Left: Topography of the active element. AFM scan of 30 × 30 µm^2 area of a 10 µm wide constriction in a 48 nm thin silver film. Right: Expansion of active element due to applied voltage V(t), as defined above, for a current density of 44 mA/µm^2. Both scans are 512 × 512 pixels yielding a spatial step size of 58.7 nm.

data is well represented by this fit function. The data shown in Figure 10 corresponds to the profile shown on the bottom left of Figure 11. The data has been translated along the x-direction so as to centre the peak of the fit at 0 µm for the purposes of visualisation. The area of the element is shown by the shaded region labelled "Constriction area" in Figure 10. From this shaded region we can see that the Voigt fit is centered slightly to the side of the centre of the element. This difference has been attributed to asymmetries in the fabricated structure resulting from the machining process [5].

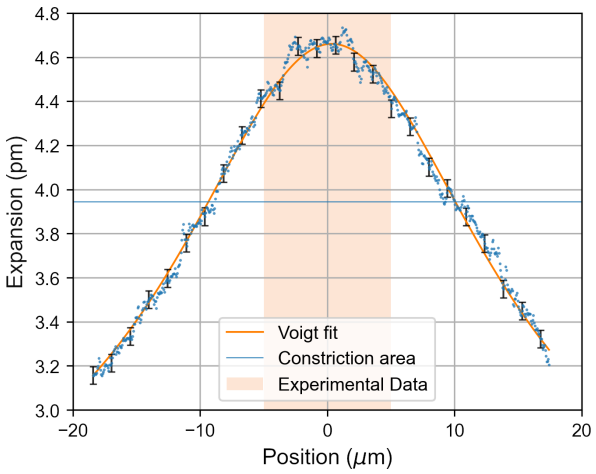

Figure 10: Experimental data showing the expansion profile for a 45.0 mA/µm^2 modulation and relative fitting with a Voigt function. The shaded area corresponds to the surface of the constriction. The position along x was shifted so to have the distribution centered around 0 for visualisation purposes. Estimated errors on the SJEM measurement are shown every twenty-fifth data point.

As with the enhanced SPR measurements above, the effect of varying current has been investigated through repeated SJEM measurements under differing applied $V(t)$. Figure 11 shows the results of these measurements. The images at the top show the spatially resolved thermal expansion across the active plasmonic element. The plots below show line profiles through the centre of the element at each current density. The shared y-axis allows for the comparison of expansion values measured at each current density. As the current density increases, the expansion of the element is seen to increase. This is in line with expectations as the temperature of the element should increase with increasing current density through the element. It should be noted that the positive x-direction here is moving from top to bottom along the profiles shown on the SJEM images in Figure 11. As expected, raising the current causes an expansion of the element in each case. Additionally, the thermal distribution broadens as the temperature of the element increases. The following detailed FEM simulations were used to verify the above results and can additionally be utilised to extract absolute temperatures from the dynamic SJEM measurements.

In Figure 12, we see the thermal effects of the modulated current across the structure under analysis simulated through COMSOL Multiphysics. As described in the first panel, the highest temperature region is clearly localised in the neighbourhood of the restriction, and the distribution spreads across the surrounding area following a profile with a FWHM ≈17.7 µm. This is more clearly depicted in Figure 12d, illustrating the temperature profile as a function of the x-coordinate. For comparison, Figure 10 shows an equivalent profile obtained experimentally for a 10 × 10 µm^2 structure with FWHM ≈19.4 µm. The

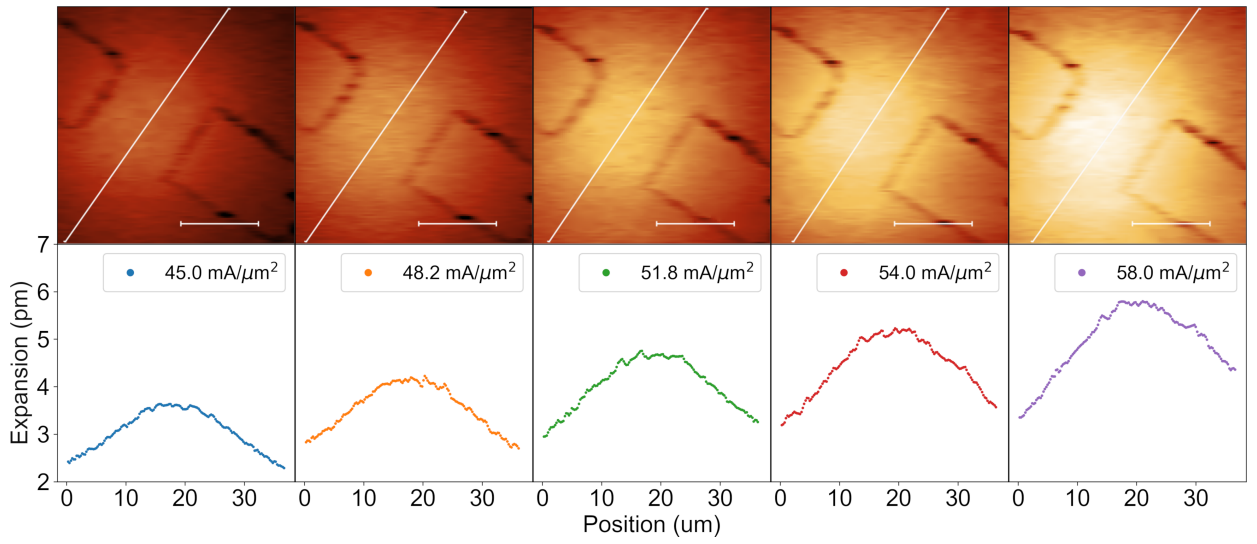

Figure 11: Thermal expansion of active element at varied current densities of 45.0, 48.2, 51.8, 54.0, and 58.0 mA/μm^2. Accompanying line profiles show expansion along the centre, represented by white lines shown in the SJEM images, of the element. The scale bars provided on the SJEM Images are 10 μm wide. Errors are assumed to be the same as shown in Figure 10 for all measurements shown.

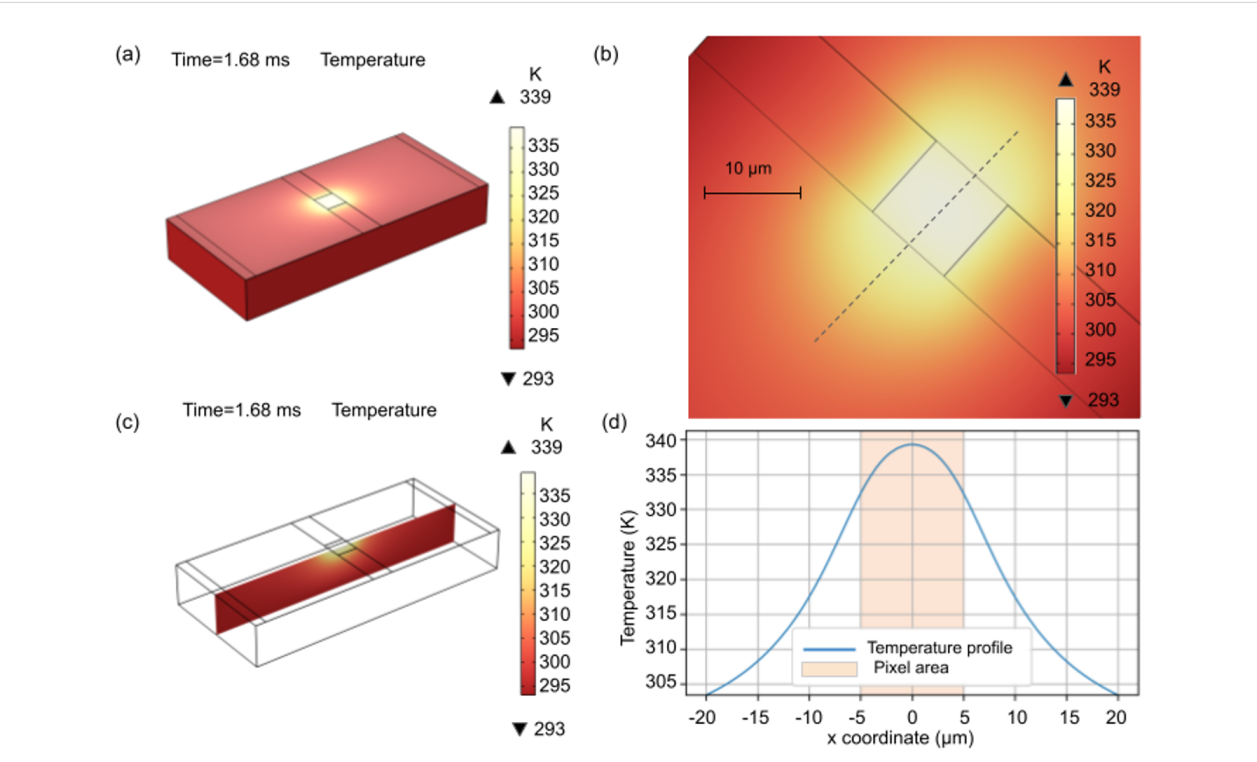

Figure 12: Results of thermoelectrical simulations done with COMSOL. (a) Surface temperature distribution for the whole structure and (b) in the neighbourhood of the constriction. (c) Temperature distribution on the *xz*-surface at *y* = 0 and (d) temperature distribution profile along the *x*-direction.

simulation results for the thermoelectrical effects are in line with the experimental results observed through AFM detection of thermal expansion, showing the same distribution, and similar FWHM, as Figure 10.

Discussion

This research characterises an active microscale optical element which can be electrically controlled. The resulting responses of the systems were investigated using two experi-

mental approaches. First, a homodyne detection enhanced SPR setup was used to provide access to the modulation of the electric field. This method provides access to the modulation of the electric field induced by varying Joule heating. Second, the spatially resolved thermal distribution of the active plasmonic element and the surrounding environment was measured through the use of SJEM. This information is required to fully model the spatial distribution of the induced electric field changes.

While this investigation focused on the behaviour of a single active plasmonic element, the combination of high localisation and the ability to modulate individual plasmonic elements at unique frequencies enables the design of arrays of such active elements which can be operated simultaneously. This could be applied to arrays of elements whose size and pitch is below the diffraction limit of light enabling sub-diffraction-limit applications.

As before, a combination of experimentally verified simulations and direct investigations through SJEM allows various parameters to be analysed, such as the exact geometry and corresponding localisation. This aids in optimisation with the aim to further improve on physical constraints.

Both experimental methods, along with simulations, provide the basis for an optimised design of the discussed active plasmonic element giving access to a variety of possible applications. This plasmonic element was developed to be used as a key feature in a new sub-diffraction-limit imaging technique currently under development.

Conclusion

In summary, using correlative methods to investigate a single device provides complementary information about desirable material properties intrinsic to the active plasmonic element. Only the combination of both experimental methods discussed here provides the complete set of information required for an optimised design of the element.

Acknowledgements

We would like to acknowledge Conor O'Donnell and Conor Foy for their insights and technical expertise during the development of this research work.

Funding

The following sources of funding are acknowledged. Science Foundation Ireland Special Future Innovator Prize grant number SFI 18/FIP/3551R. The Enterprise Ireland funding grant number CF20211651. Ciarán Barron acknowledges funding from the UCD SIRAT scheme. Silas O'Toole acknowledges funding from the UCD Thomas Preston Scheme. Giulia Di Fazio and Samuel Kenny acknowledge funding from the Irish Research Council grant number GOIPG/2022/1207.

ORCID® iDs

Ciarán Barron - https://orcid.org/0000-0003-1195-3141
Giulia Di Fazio - https://orcid.org/0000-0002-7713-4301
Samuel Kenny - https://orcid.org/0000-0003-1511-8119
Silas O'Toole - https://orcid.org/0000-0003-2877-4836
Robin O'Reilly - https://orcid.org/0000-0003-1366-4976
Dominic Zerulla - https://orcid.org/0000-0001-8479-9654

References

1. Haffner, C.; Chelladurai, D.; Fedoryshyn, Y.; Josten, A.; Baeuerle, B.; Heni, W.; Watanabe, T.; Cui, T.; Cheng, B.; Saha, S.; Elder, D. L.; Dalton, L. R.; Boltasseva, A.; Shalaev, V. M.; Kinsey, N.; Leuthold, J. *Nature* **2018,** *556,* 483–486. doi:10.1038/s41586-018-0031-4
2. Krasavin, A. V.; Zayats, A. V. *Appl. Phys. Lett.* **2010,** *97,* 041107. doi:10.1063/1.3464552
3. Sorger, V. J.; Ye, Z.; Oulton, R. F.; Wang, Y.; Bartal, G.; Yin, X.; Zhang, X. *Nat. Commun.* **2011,** *2,* 331. doi:10.1038/ncomms1315
4. Fang, N.; Lee, H.; Sun, C.; Zhang, X. *Science* **2005,** *308,* 534–537. doi:10.1126/science.1108759
5. Barron, C.; O'Toole, S.; Zerulla, D. *Nanomanuf. Metrol.* **2022,** *5,* 50–59. doi:10.1007/s41871-021-00121-7
6. Otto, A. *Z. Phys.* **1968,** *216,* 398–410. doi:10.1007/bf01391532
7. Kretschmann, E.; Raether, H. *Z. Naturforsch., A: Astrophys., Phys. Phys. Chem.* **1968,** *23,* 2135–2136. doi:10.1515/zna-1968-1247
8. Gryczynski, I.; Malicka, J.; Nowaczyk, K.; Gryczynski, Z.; Lakowicz, J. R. *J. Phys. Chem. B* **2004,** *108,* 12073–12083. doi:10.1021/jp0312619
9. Hibbins, A. P.; Evans, B. R.; Sambles, J. R. *Science* **2005,** *308,* 670–672. doi:10.1126/science.1109043
10. Andrew, P.; Barnes, W. L. *Science* **2004,** *306,* 1002–1005. doi:10.1126/science.1102992
11. Bozhevolnyi, S. I.; Volkov, V. S.; Devaux, E.; Laluet, J.-Y.; Ebbesen, T. W. *Nature* **2006,** *440,* 508–511. doi:10.1038/nature04594
12. Isfort, G.; Schierbaum, K.; Zerulla, D. *Phys. Rev. B* **2006,** *73,* 033408. doi:10.1103/physrevb.73.033408
13. Isfort, G.; Schierbaum, K.; Zerulla, D. *Phys. Rev. B* **2006,** *74,* 033404. doi:10.1103/physrevb.74.033404
14. Salandrino, A. *Phys. Rev. B* **2018,** *97,* 081401. doi:10.1103/physrevb.97.081401
15. Fardad, S.; Lialys, J.; Lialys, L.; Salandrino, A. *Opt. Lett.* **2021,** *46,* 2581. doi:10.1364/ol.424355
16. Kneipp, K.; Wang, Y.; Kneipp, H.; Perelman, L. T.; Itzkan, I.; Dasari, R. R.; Feld, M. S. *Phys. Rev. Lett.* **1997,** *78,* 1667–1670. doi:10.1103/physrevlett.78.1667
17. Zerulla, D.; Isfort, G.; Kölbach, M.; Otto, A.; Schierbaum, K. *Electrochim. Acta* **2003,** *48,* 2943–2947. doi:10.1016/s0013-4686(03)00359-1
18. Ozbay, E. *Science* **2006,** *311,* 189–193. doi:10.1126/science.1114849
19. Hill, R. T. *Wiley Interdiscip. Rev.: Nanomed. Nanobiotechnol.* **2015,** *7,* 152–168. doi:10.1002/wnan.1314
20. McClean-Ilten, É.; Gordon, J.; Zerulla, D. *Phys. Rev. B* **2022,** *105,* 235413. doi:10.1103/physrevb.105.235413

21. Barnes, W. L.; Dereux, A.; Ebbesen, T. W. *Nature* **2003,** *424,* 824–830. doi:10.1038/nature01937
22. Krasavin, A. V.; Zheludev, N. I. *Appl. Phys. Lett.* **2004,** *84,* 1416–1418. doi:10.1063/1.1650904
23. O'Toole, S.; Zerulla, D. *Materials* **2020,** *13,* 4753. doi:10.3390/ma13214753
24. Rehwald, S.; Berndt, M.; Katzenberg, F.; Schwieger, S.; Runge, E.; Schierbaum, K.; Zerulla, D. *Phys. Rev. B* **2007,** *76,* 085420. doi:10.1103/physrevb.76.085420
25. Sundari, S. T.; Chandra, S.; Tyagi, A. K. *J. Appl. Phys.* **2013,** *114,* 033515. doi:10.1063/1.4813874
26. Yeshchenko, O. A.; Bondarchuk, I. S.; Gurin, V. S.; Dmitruk, I. M.; Kotko, A. V. *Surf. Sci.* **2013,** *608,* 275–281. doi:10.1016/j.susc.2012.10.019
27. Winsemius, P.; van Kampen, F. F.; Lengkeek, H. P.; van Went, C. G. *J. Phys. F: Met. Phys.* **1976,** *6,* 1583–1606. doi:10.1088/0305-4608/6/8/017
28. Reddy, H.; Guler, U.; Chaudhuri, K.; Dutta, A.; Kildishev, A. V.; Shalaev, V. M.; Boltasseva, A. *ACS Photonics* **2017,** *4,* 1083–1091. doi:10.1021/acsphotonics.6b00886
29. Harris, D. C.; Johnson, L. F.; Cambrea, L. R.; Baldwin, L.; Baronowski, M.; Zelmon, D. E.; Poston, W. B.; Kunkel, J. D.; Parish, M. V.; Pascucci, M. R.; Gannon, J. J., Jr.; Wen, T.-C. *Opt. Eng. (Bellingham, WA, U. S.)* **2017,** *56,* 077103. doi:10.1117/1.oe.56.7.077103
30. DeFranzo, A. C.; Pazol, B. G. *Appl. Opt.* **1993,** *32,* 2224. doi:10.1364/ao.32.002224
31. Raether, H. *Surface plasmons on smooth and rough surfaces and on gratings;* Springer: Berlin, Heidelberg, 1988. doi:10.1007/bfb0048317
32. Majumdar, A.; Varesi, J. *J. Heat Transfer* **1998,** *120,* 297–305. doi:10.1115/1.2824245
33. Johnson, P. B.; Christy, R. W. *Phys. Rev. B* **1972,** *6,* 4370–4379. doi:10.1103/physrevb.6.4370
34. Thomas, M. E.; Andersson, S. K.; Sova, R. M.; Joseph, R. I. *Infrared Phys. Technol.* **1998,** *39,* 235–249. doi:10.1016/s1350-4495(98)00010-3
35. Wu, Y.; Zhang, C.; Estakhri, N. M.; Zhao, Y.; Kim, J.; Zhang, M.; Liu, X.-X.; Pribil, G. K.; Alù, A.; Shih, C.-K.; Li, X. *Adv. Mater. (Weinheim, Ger.)* **2014,** *26,* 6106–6110. doi:10.1002/adma.201401474

License and Terms

BEILSTEIN JOURNAL OF NANOTECHNOLOGY

Exploring internal structures and properties of terpolymer fibers via real-space characterizations

Michael R. Roenbeck*[1,2] and Kenneth E. Strawhecker[2]

Full Research Paper

Open Access

Address:
[1]Department of Marine Engineering, U.S. Merchant Marine Academy, Kings Point, New York 11024, United States and [2]DEVCOM, Army Research Laboratory, Aberdeen Proving Ground, MD, 21005, United States

Email:
Michael R. Roenbeck* - roenbeckm@usmma.edu

* Corresponding author

Keywords:
atomic force microscopy; correlative characterization; high-performance fibers; structure–property relationships; Technora®

Beilstein J. Nanotechnol. **2023,** *14,* 1004–1017.
https://doi.org/10.3762/bjnano.14.83

Received: 25 May 2023
Accepted: 21 September 2023
Published: 05 October 2023

This article, co-edited by the guest editor M. Mail, is part of the thematic issue "Correlative approaches in materials science – from the micrometer to the nanometer scale".

Associate Editor: J. J. Schneider

Abstract

While significant research has investigated the processing and properties of high-performance terpolymer fibers, much remains to be understood about the internal nano- and microstructures of these fibers, and how these morphologies relate to fiber properties. Here we use a focused ion beam notch technique and multifrequency atomic force microscope mapping to characterize the internal structure and local mechanical properties within Technora® fibers. We find a highly fibrillated structure that appears to connect with both the fiber's molecular chemistry and full-fiber mechanical properties. In addition, through detailed comparisons with Kevlar® K29 fibers, we find remarkable differences between the internal structures of the two fibers, and posit connections between our measurements and multifunctional performance studies from the literature.

Introduction

High-performance polymer fibers have enabled groundbreaking advancements in numerous applications, from personal armor to tires to sports equipment, that aim to maximize mechanical performance while minimizing weight. The successes achieved with forerunners in the field, such as Kevlar® and ultrahigh molecular weight polyethylene (UHMWPE), have driven tremendous interest in new fiber chemistries and processing techniques. The development of Technora® in 1987 marked a new approach to polymer fiber design, with an emphasis on aligning extended molecular chains rather than optimizing crystallites. This strategy aimed to explore new chemistries that could enhance multifunctional aspects of fibers without adversely affecting fiber mechanical properties. Indeed, in developing Technora®, Teijin Ltd. had four principal aims: to manufacture a (i) cost-effective fiber with (ii) similar mechanical properties to Kevlar® that was (iii)

heat-resistant and (iv) soluble in organic solvents [1]. A highly oriented fiber structure exhibiting these characteristics was achieved through a terpolymer chemical formulation, consisting of terephthaloyl chloride (TPA), *p*-phenylenediamine (PPD), and 3,4′-diaminodiphenyl ether (DPE) (Figure 1a). Compared to Kevlar®, which includes 50% concentrations of the first two monomers alone (forming *p*-phenylene terephthalamide (PPTA)), the molecular structure of Technora® substitutes DPE for half of the PPD monomers [1-5]. Of course, this distinction in fundamental chemistry has significant implications for the structures and properties of the resulting fibers.

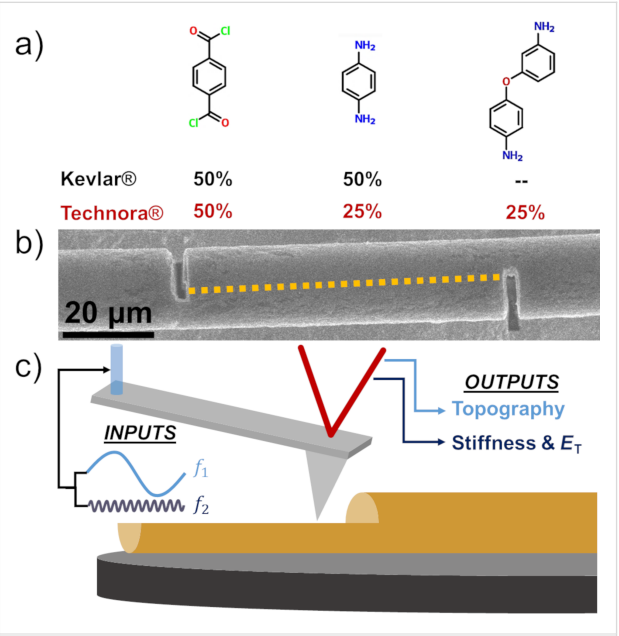

Figure 1: Materials and methods overview. (a) Three primary monomers utilized in Technora® fibers: terephthaloyl chloride (TPA), *p*-phenylenediamine (PPD), and 3,4′-diaminodiphenyl ether (DPE), from left to right in the ratios shown [1-4]. Corresponding percentages also shown for Kevlar®. (b) Micrograph of a FIB-notched Technora® fiber. Dashed line highlights a shear plane between the two notches. The fiber readily opens along this plane, exposing internal fiber surfaces for characterization. (c) Multifrequency AFM schematic. A cantilever is driven by a blue laser that simultaneously excites the cantilever at its first and second resonance frequencies (f_1 and f_2). The response of the cantilever as it scans across the exposed internal fiber surface provides information about the local fiber internal morphology and mechanical response (stiffness and transverse elastic modulus (E_T)).

To date, structure–property characterizations of Technora® in the literature have primarily focused on (i) X-ray diffraction (XRD), (ii) nuclear magnetic resonance (NMR) spectroscopy, and (iii) fiber tensile properties. Interestingly, although Technora® is noncrystalline, it can be effectively modeled through XRD as a paracrystalline material such as Kevlar®. Within this framework, the Technora® paracrystalline distortion parameter, a measure of crystalline "sinuosity", was lower (i.e., indicated better alignment) than in all Kevlar® classes explored in a study by Wu and Blackwell [3]. In characterizing the lateral molecular organization in Technora® from XRD, the researchers carefully noted that the broad lateral apparent crystallite "peak" in Technora® was likely not a single peak, but rather an aggregation of many individual peaks [3]. Ferreira et al. made similar observations from XRD and concluded that this broad peak reflected an "ordered but not crystalline" fiber structure [6]. In addition, analytical modeling of XRD spectra suggested that the three principal monomers that comprise Technora® are randomly sequenced, a conclusion later supported by extensive NMR studies [2,5]. Despite this highly unique chemical structure, research has shown that Technora® and Kevlar® K29 fibers possess similar elastic moduli and tensile strengths [6,7]. These studies also show that Technora® exhibits a narrower distribution in tensile strength, as well as greater creep and fatigue resistance [6,7]. Separate studies of fiber multifunctional properties also showed that Technora® exhibits resistance to moisture and chemical degradation [1,8].

The aforementioned studies have provided critical insights into the structure–property relationships of Technora® fibers. However, our understanding of Technora® would greatly benefit from direct, real-space characterization of the internal structures of these fibers. Real-space measurements could effectively integrate observations of features at different length scales and verify the applicability of analytical structural models used to date. Over the last several years, a "focused ion beam (FIB) notch" technique has been developed and employed to address these gaps in understanding of the internal structures of fibers such as Kevlar® and UHMWPE [9-13]. Here we extend this technique to Technora® by notching individual fibers (Figure 1b), gently opening them along shear planes to expose internal surfaces, and then scanning across those surfaces using an atomic force microscope (AFM) (Figure 1c). AFM scans yield internal nano- and microscale topography, stiffness, and transverse elastic modulus (E_T) maps of internal structural features and local mechanical responses in real space. (See the Experimental section for additional details.) As Technora® has often been compared to Kevlar® K29 fibers, we focus further on comparing the internal structures of these two fiber classes and relate our observations to extensive mechanical testing reported in the literature. Our findings shed new light on the unique interior morphologies of Technora® terpolymer fibers and, in turn, highlight important considerations for the development of future classes of high-performance fibers.

Results

AFM characterizations of Technora®

AFM maps enable direct characterization of both fiber nano- and microstructures in real space. Large-scale maps span across

the fiber diameter to highlight prominent microstructural features. For Technora®, both the topography and stiffness maps (Figure 2) revealed a consistent microstructure across the fiber diameter at this length scale. Complementing topography and stiffness maps, lateral line profiles (e.g., dashed line, Figure 2a) quantified both topography and stiffness variations across the diameter. Topography and stiffness (Figure 2c) were remarkably uniform across the diameter as well.

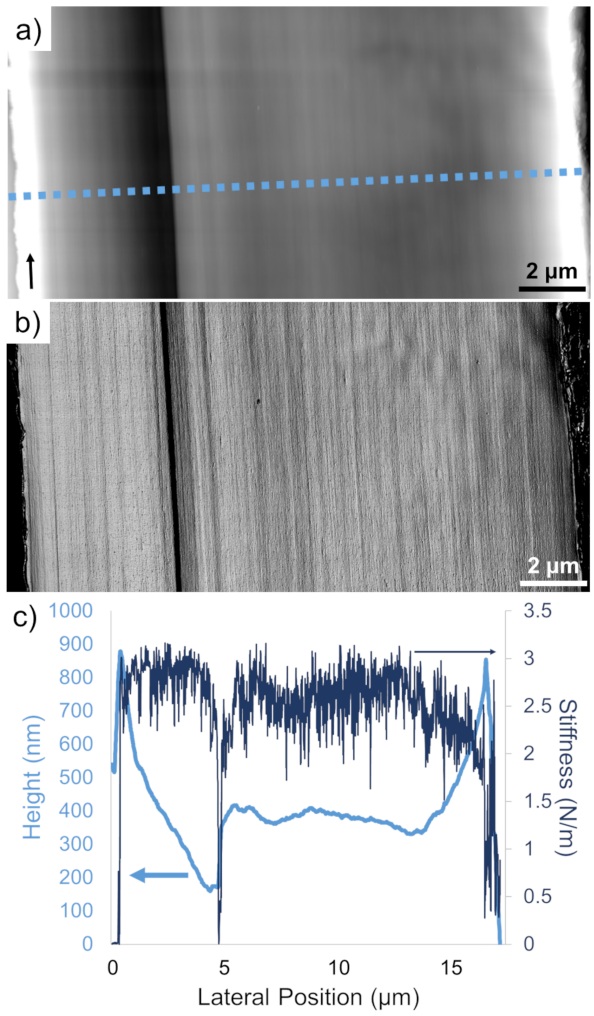

Figure 2: Fiber-wide Technora® AFM maps. (a) Topography map across a full fiber cross section. The arrow (bottom left) denotes the longitudinal direction (i.e., fiber axis direction), while the lateral dashed line denotes the line profile in (c). (b) Stiffness map across a full fiber cross section. (c) Representative lateral topography and transverse stiffness line scans (bright and dark lines, respectively).

Only two notable features deviate from our consistent topography and stiffness measurements: (i) slopes from the outer edges inward and (ii) a sudden jump at a lateral position of ca. 5 µm. It should be noted that the slopes are very shallow in real space, with height variations of ca. 700 nm or less spanning several micrometers along the diameter. The sudden jump correlates precisely with the lone compliant (dark) longitudinal band in the stiffness map. Based on comparisons with other fibers, we expect that these features resulted from the way this particular fiber split open after FIB notching. Likewise, the lone drop in stiffness makes sense, as the AFM probe experiences a local reduction in tip–substrate contact area. However, similar topography and stiffness jumps forming a compliant band were not observed elsewhere in the fiber.

Topography and stiffness maps also reveal constituents throughout the microstructure that preferentially align with the main fiber axis, as parallel longitudinal lines on topography and stiffness maps can be traced from the top to the bottom of each map. No apparent skin–core differentiation in the microstructure (e.g., as in Kevlar®) is observed [11,13-16]. The lack of evidence for a skin–core structure in Technora® was referenced in an earlier study by Derombise et al. [17], but to our knowledge, this is the first time this has been directly shown through real-space mapping.

Complementing these full-fiber scans, high-resolution topography and stiffness maps on smaller fiber subdomains were also obtained to study the nanostructure of Technora®. From detailed topography maps, we found that the well-aligned surface features observed on the full-diameter map were fibrillar in structure (Figure 3a). The surface consisted of a branched network of fibrils closely aligned to the fiber axis, as highlighted in Figure 3b. The widths of individual fibrils varied substantially (20–45 nm) along their length. Unlike in other polymer fibers we have explored to date, in Technora®, these features regularly merge and separate from one another, intersecting at nodes and splitting off into fibrils with distinct dimensions [9-13]. Likewise, some fibrils appear to protrude into and out from the primary surface exposed by FIB notching, suggesting that this branched network exists in three dimensions within the fiber.

Combining these topographical observations with stiffness maps (Figure 3c), a few important features emerged. Along the fiber axis, we observed longitudinal bands of high topography and, nearby, longitudinal bands of low stiffness. Stiffness maps also revealed bands of high stiffness spanning hundreds of nanometers laterally (i.e., left-to-right in each map), along with slightly elevated topographical ribbons. To assess the repeatability of these measurements, we analyzed several nanoscale maps in other representative regions of Technora® fibers and compared trace and retrace profiles (Figure 4). One example is highlighted in the red box (Figure 4a,c) that corresponds to the red shaded part of the profile measurements (Figure 4b,d). Additional examples of these observations in the profiles are highlighted in blue but not imposed on the AFM maps for clarity. In

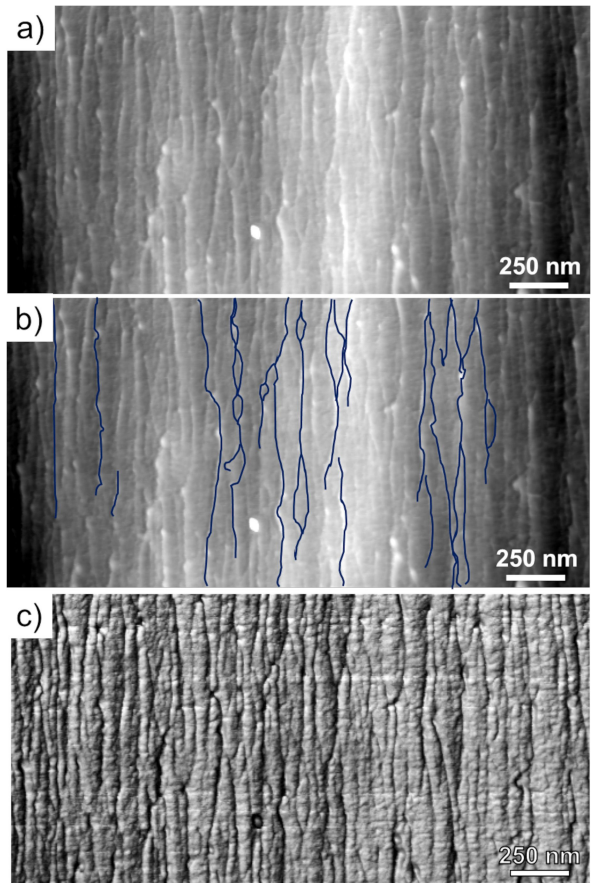

Figure 3: AFM maps of the internal nanostructure within a Technora® fiber. (a) Topography map, 2.5 × 1.25 µm. (b) Copy of the topography map with selected fibrils marked in blue highlighting the branched structure of fibrils aligned with the fiber axis. (c) Stiffness map of the same domain. Scale ranges for each scan are approximately (a, b) 0–12 nm and (c) 0.5–2.5 N/m dark to light.

each highlighted region, there was clearly a correlation between topography and stiffness, but the precise nature of this correlation required higher resolution analysis of line profiles.

From lateral profiles such as Figure 5a, we observed that domains with high topography directly corresponded to high stiffness. Those lateral profiles indicate that low-stiffness longitudinal bands in the red boxes in Figure 4 do not coincide precisely with the fibrils; instead, they are slightly offset. The manner in which these compliant regions are offset from the fibrils appears to be random. They are not consistently to the left or right of the fibrils, and the offset persists regardless of the AFM probe scanning direction (i.e., trace or retrace, Figure 4). In longitudinal line scans (Figure 5b), we found the same topography–stiffness correlation. Topographically high regions were also stiff. This profile confirms what appear as "ladder rungs" in the blue boxes, supporting the presence of a branched network. These off-axis structures appear fainter than the axial fibrils because of their smaller relative changes in stiffness and height. Finally, to probe the nature of the nodes between branches in the fibril network, we obtained profiles across nodes as well (Figure 5c). Clearly, nodes are substantially taller (ca. 5 nm) than other features along both the longitudinal and lateral directions (1–2 nm), reflecting the fact that discrete fibrils merge. The locally elevated stiffness also reaches the same value as individual fibrils and "ladder rungs". As the stiffness of the material indirectly reflects the underlying structure, these comparable stiffness values suggest that the material organization in nodes matches that within individual fibrils. Together, these findings provide quantitative details about the branched network of fibrils that defines the nanostructure of Technora®.

Technora® vs Kevlar® K29

To further highlight the unique internal nanostructure of Technora®, we compare topography and stiffness maps of Technora® to the more widely studied Kevlar® K29 [9,11-13]. In particular, we focus on representative 1 µm × 1 µm subdomains inside fibers from each class. In topography maps (Figure 6a), Kevlar® possesses well-packed, distinguishable, 20–25 nm wide fibrils that align closely with the fiber direction. Sharp lateral variations in topography in the lateral direction are observed, akin to vertical steps from left to right, which indicate the interfaces between adjacent fibrils. Fibrils also oscillate with respect to the fiber axis, both laterally and "vertically" (i.e., into and out of the surface plane), reflecting the well-known pleated sheet microstructure within Kevlar® [14]. In contrast to this morphology, Technora® (Figure 6b) shows thin, separated fibrils that are not arranged in close concert with one another. Various fibrils exhibit small oscillations with respect to the fiber axis and protrude into and out of the underlying surface, suggesting a random misorientation of constituents compared to the densely packed and well-oriented sets of fibrils in Kevlar®. The aforementioned "branched network" of fibrils is also apparent in Technora® but not in Kevlar®.

Comparing corresponding stiffness maps over each domain provides additional insights into these fiber nanostructures. Fibrils in Kevlar® stiffness maps (Figure 6c) were clear with compliant longitudinal bands at the interfaces between adjacent fibrils. In addition, gradations in transverse stiffness were observed in the longitudinal direction, coinciding with adjacent pleat components in the microstructure (ca. every 250 nm along the fiber axis) [11,13,14]. However, Technora® stiffness maps over the same area (Figure 6d) exhibited "mosaic" topography and stiffness maps.

To further characterize and compare these nanostructural features in Kevlar® and Technora®, we quantitatively analyzed both lateral and longitudinal line scans within each of these

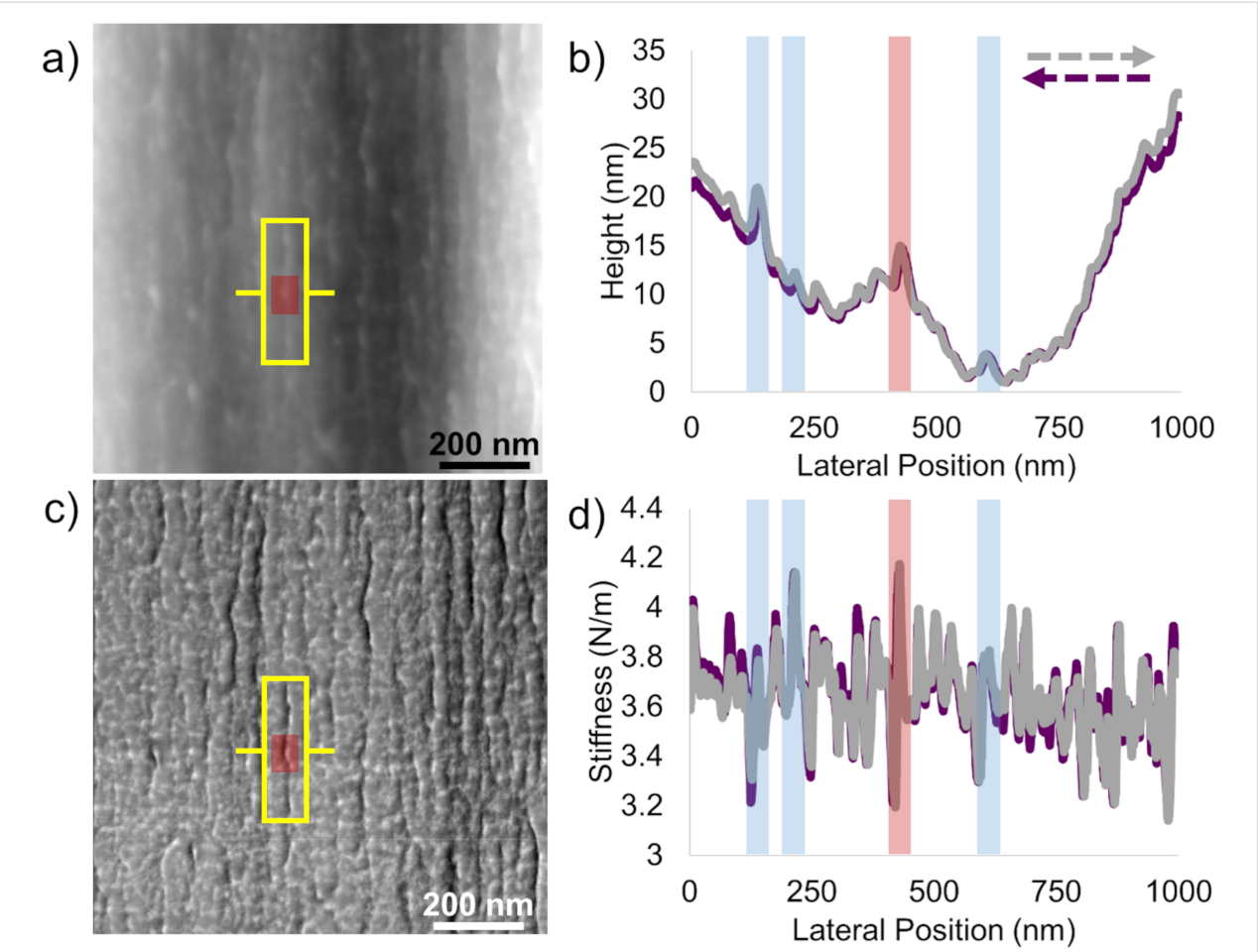

Figure 4: Quantitative AFM maps of internal Technora® fiber nanostructures. (a) Topography map of 1 μm × 1 μm region within a Technora® fiber. (b) Left-to-right trace and retrace line scans through the red box in (a). The peak shaded in red corresponds to the prominent fibril highlighted in (a), while peaks shaded blue highlight repeated observations in other peaks. (c) Stiffness map over the same 1 μm × 1 μm region. (d) Stiffness trace and retrace profiles corresponding to the topography profiles in (b).

maps. Lateral topography line scans in Kevlar® (Figure 7a) showed sharp jumps of up to tens of nanometers near fibril interfaces, likely reflecting interfaces between "stacks" of fibrils [11,18]. In contrast, Technora® lateral topography scans over the corresponding domains were much flatter, with roughly an order of magnitude smaller fluctuations in height. Similar results were found in longitudinal topography profiles (Figure 7b), that is, Technora® structural variations along the fiber axis were substantially lower than those in Kevlar®. Whereas the out-of-plane pleated sheet microstructure in Kevlar® introduces topological variations of tens of nanometers along the fiber direction, Technora® profiles were smooth and lacked prominent microstructural motifs.

Closely related observations can be made from stiffness maps of the two fibers. From lateral profiles (Figure 7c), Kevlar® transverse stiffness at fibril interfaces dropped down to ca. 90% of the mean stiffness value. While longitudinal Kevlar® transverse stiffness variations (Figure 7c) were not as significant as lateral variations, they still varied up to ±60% of the mean and correlated well with components of the "pleated sheet" internal structure [11,13,14]. In contrast, maximum variations in Technora® transverse stiffness were less than ±15% of the mean both laterally and longitudinally and showed no recurring patterns in stiffness variations.

Transverse elastic modulus quantifications

We present these last results as relative stiffness variations because multiple AFM tips needed to be used to survey these multiple subdomains. Monitoring tip wear is cumbersome when targeting a broad survey of different regions of multiple fibers, so the results above only reflect a semi-quantitative, relative comparison. To complement these qualitative comparisons, we also quantitatively compared the transverse elastic modulus (E_T) obtained on suitable subdomains within Technora® and Kevlar® K29 fibers.

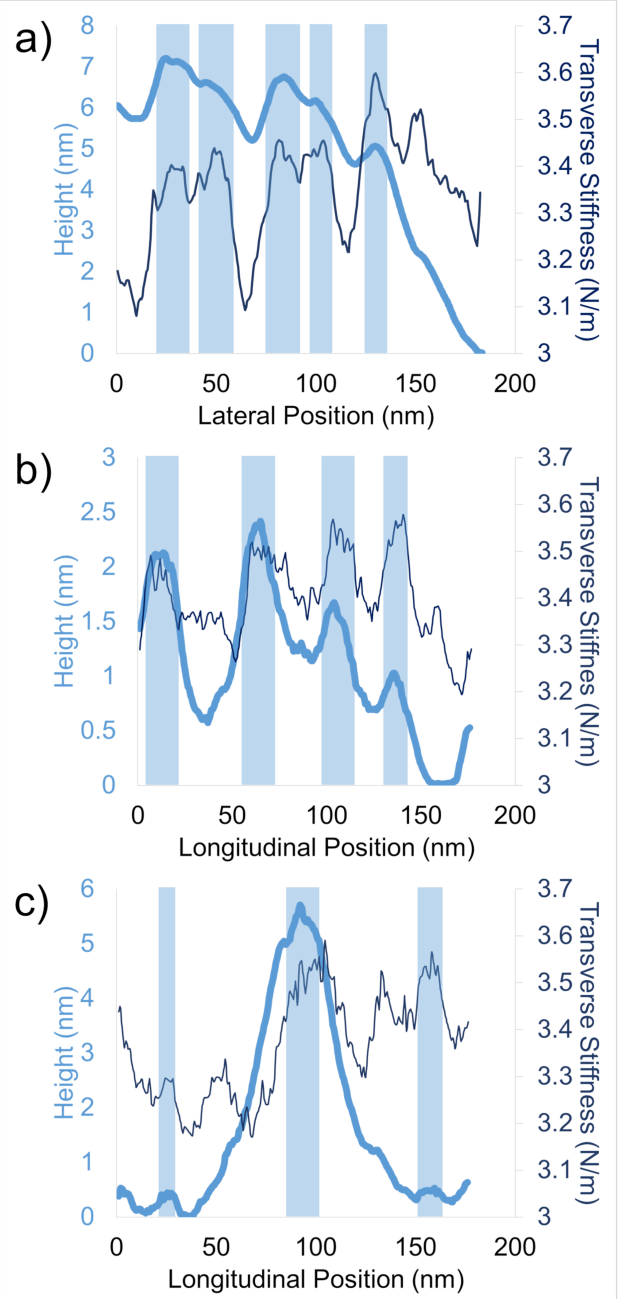

Figure 5: Nanoscale topography–stiffness profile correlations. (a) Representative lateral line scan. (b) Representative longitudinal line scan. (c) Longitudinal line scan over a node. Thick light lines correspond to topography (height), while thin dark lines denote transverse stiffness. In all cases, shaded boxes highlight correlations between locally elevated topography domains and increases in transverse stiffness.

Figure 8 highlights aggregate frequency distributions in transverse elastic modulus (bold top lines) and individual distributions (lower lines) obtained from multiple subdomains of Technora® and Kevlar® K29 fibers. In Technora®, individual distributions (i.e., distributions within any one region) were narrow with clear peaks (Figure 8a). While several scans showed frequent readings near 2.6 GPa, E_T centered around 1.5–1.6 GPa in most scans. Taken together, this led to a total distribution with a mean of 2.00 GPa and a mode (i.e., highest peak) of 1.53 GPa. In contrast, K29 individual distributions (Figure 8b) appeared as plateaus ranging from 0.5 to 3.5 GPa. When present, shallow peaks in K29 arose near these upper and lower limits, resulting in a plateau in the overall frequency distribution. The mean for K29 was 2.18 GPa. The mode of this total K29 distribution was 2.79 GPa, though a second peak near 1.1 GPa was virtually as likely to occur based on this distribution.

Figure 8c isolates each total distribution to facilitate direct comparisons between them. In addition, vertical shaded boxes in Figure 8c indicate the mean values from full-fiber transverse compression experiments reported in the literature for each fiber class (2.68 GPa for Kevlar®, 1.64 GPa for Technora®) [8,19]. These average values coincide very closely with the modes of each distribution from our nanoscale AFM measurements.

Discussion

In this study we have, for the first time, isolated and directly characterized the internal structures of Technora® fibers using AFM. Here we elaborate and contextualize several aspects related to our findings. First, we describe how this real-space characterization provides new information about the Technora® fiber nanostructure. We then focus on fiber microstructures, highlighting how this technique expands upon conclusions from previous studies. Lastly, we comment on how characterizing the structural composition in real space relates to Technora® performance parameters. In particular, through comparisons with the Kevlar® K29 structure, we discuss structure–property relationships that explain the mechanical properties of these two fibers. We also analyze several critical multifunctional performance parameters highlighted by the developers of Technora® and explore how they relate to the fiber structures. Together, we believe these analyses help elucidate structure–property relationships within high-performance polymer fibers.

Technora® nanostructure

In terms of the Technora® nanostructure, our measurements directly reveal two key motifs: (i) the presence of nanoscale fibrils that are well aligned with respect to the fiber axis and form a branched network and (ii) nanoscale domains with high local transverse stiffness. Through WAXD studies, Ferreira et al. deduced that Technora® fibers are “ordered but not crystalline” [6]. This conclusion aligned well with corresponding WAXD and NMR studies, which indicated that the molecules within Technora® include random monomer sequences [2,3,5]. Adjacent extended-chain molecules would not be able to form crystallites, as random sequences of molecules including the DPE monomer (which locally changes chain orientation) would

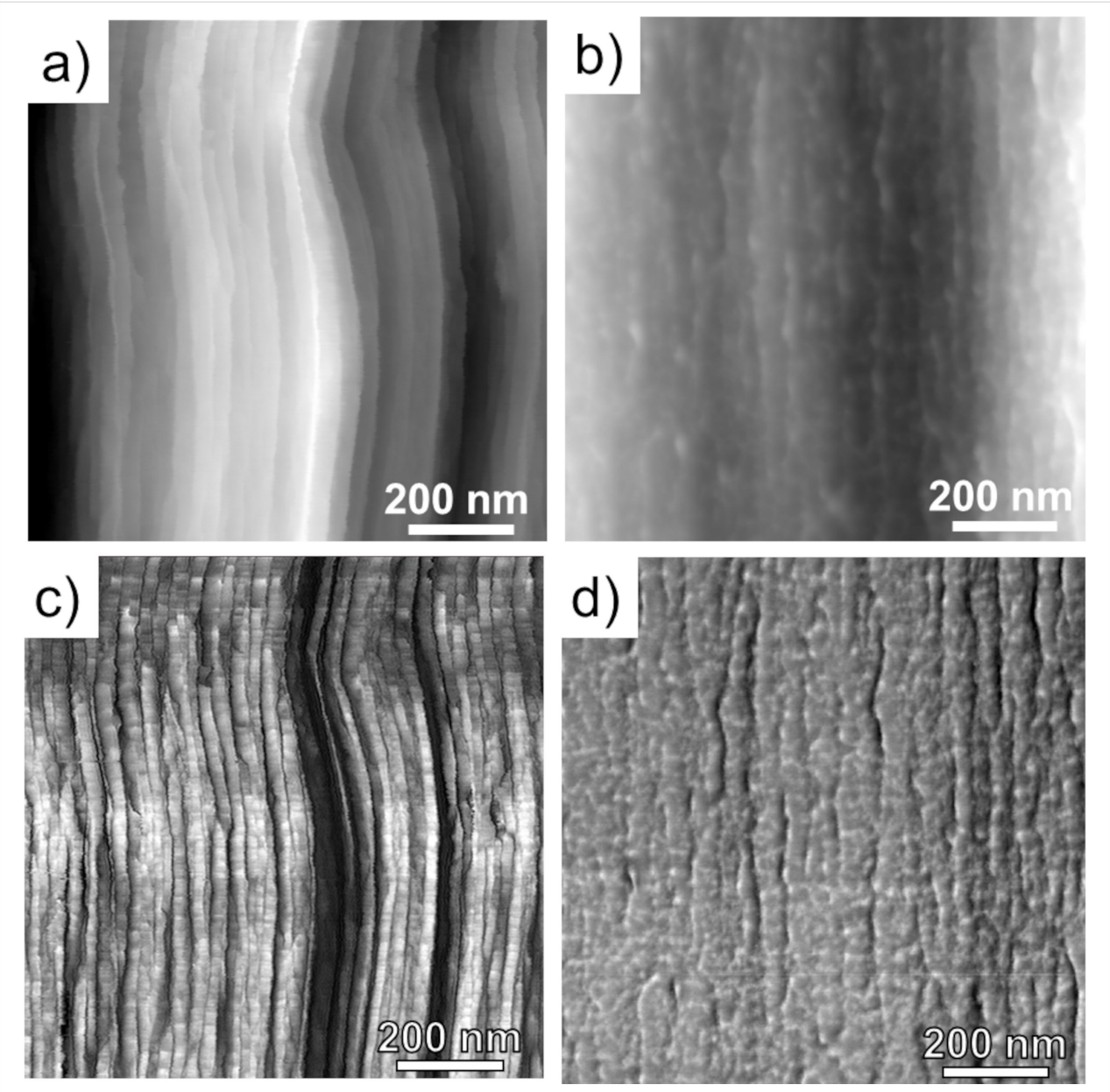

Figure 6: Internal AFM maps of Kevlar® K29 vs Technora®. (a, b) Topography maps of Kevlar® and Technora®, respectively. (c, d) Corresponding transverse stiffness maps of Kevlar® and Technora®, respectively. Scale ranges for each scan are approximately (a) 0–200 nm, (b) 0–30 nm, (c) 0–0.2 N/m, and (d) 2.6–4.4 N/m dark to light. Figure 6c was adapted from [12] (© 2018 E. Sandoz-Rosado et al., distributed under the terms of the Creative Commons Attribution 4.0 International License, https://creativecommons.org/licenses/by/4.0/).

prevent neighboring molecules from forming cohesive extended crystals. This would lead to a mixture of ordered and disordered subdomains with varying alignment, as schematized in Figure 9. Nevertheless, Ozawa hypothesized that well-aligned, extended chain molecules consisting of 50% PPTA concentration could still effectively transfer applied loads between adjacent chains [1].

These previous characterizations of the molecular chemistry of Technora® appear to explain the branched network of nanoscale fibrils we observe. Despite the randomly sequenced terpolymer chemistry, nanoscale fibrils still clearly form in Technora®. The branched network likely results from local variations in the strength of intermolecular interactions. For example, misalignment between adjacent molecules (e.g., due to molecular "bends" within DPE molecules) or weak intermolecular interactions (e.g., due to distributions in monomers capable of intermolecular hydrogen bonding) may make it energetically favorable for sets of molecules to branch apart at different junctures rather than to remain together within a fibril. These unique

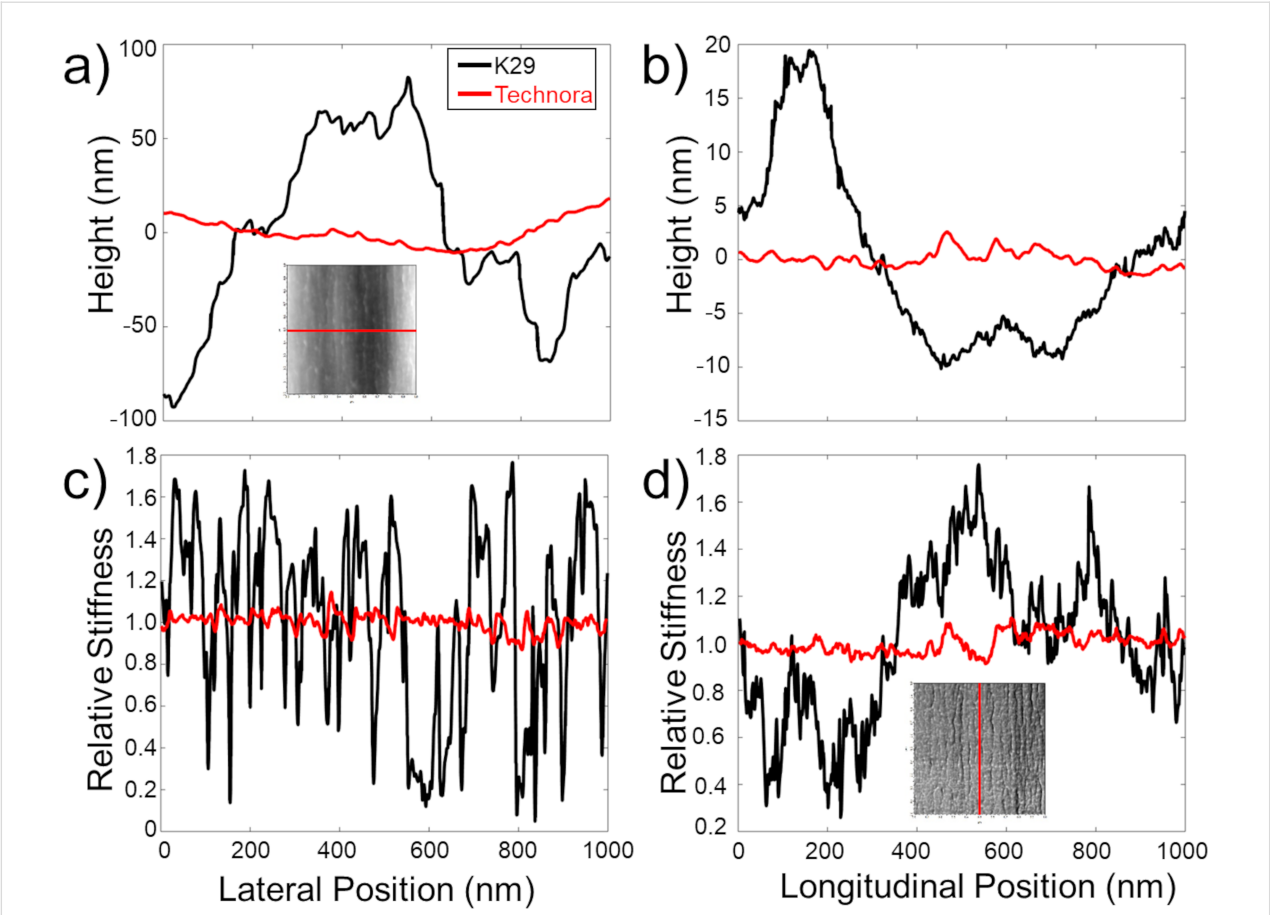

Figure 7: Line profiles across Kevlar® and Technora® subdomains. (a) Overlaid lateral profiles in Kevlar® K29 and Technora® across topographical maps. The inset highlights the line in the Technora® topography map corresponding to the profile shown. (b) Representative longitudinal topographical line scans within the same maps. (c) Lateral line scans of transverse stiffness, corresponding to the topographical scans in (a). (d) Longitudinal transverse stiffness scans corresponding to lines in (b). The inset highlights the vertical line in the Technora® stiffness map.

molecular structures cannot lead to a truly crystalline fiber, but evidently, they are still strong and concentrated enough to form the nanoscale fibrils we repeatedly observe throughout Technora® fibers.

At the same time, a random monomer sequence should result in a heterogeneous map of transverse stiffness within the material. Here the stiffness maps of Technora® sharply contrast with those of Kevlar®. In Kevlar®, the primary observable nanostructural features are sets of adjacent fibrils with well-defined, compliant interfaces (Figure 6). In Technora®, both lateral and longitudinal line scans (Figure 5a,b) show that elevated fibrils exhibit high transverse stiffness. This high stiffness suggests that the material within Technora® fibrils is well-ordered, that is, lacking compliant nanoscale subdomains that may arise from voids, mismatched molecules, or other defects. Furthermore, line scans across nodes (Figure 5c) show virtually the same stiffness as neighboring fibrils, indicating that these nanoscale features can merge and separate without affecting transverse mechanical responses. Overall, our nanoscale characterizations of AFM topography and stiffness maps corroborate earlier findings that suggested Technora® possesses (i) repeated longitudinal features along the crystalline axis and (ii) a broad distribution of apparent lateral crystallite sizes, implying an ordered but non-crystalline structure [3,6]. Moreover, we directly uncover fibril constituents within Technora® fibers and relate their nanoscale structures to previous studies of the fibers' fundamental chemistry.

Technora® microstructure

We can also use our real-space AFM scans to highlight two observations regarding the microstructure of Technora® fibers. First, WAXD studies previously suggested that Technora® does not possess the same degree of "three-dimensional order" as Kevlar® [3]. Our line scans over representative 1 μm × 1 μm regions of Technora® and Kevlar® fibers (Figure 7) support this analysis. Discrete fibrils can be clearly traced throughout the core microstructure of Kevlar®. At fibril interfaces, we see

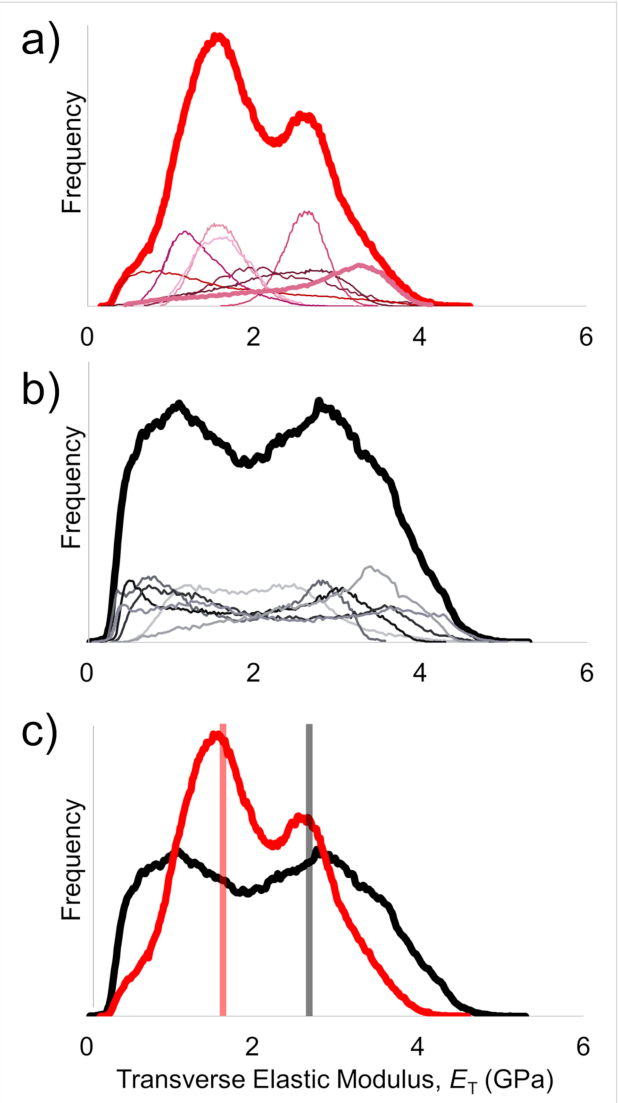

Figure 8: Transverse elastic modulus distributions from multifrequency AFM scans. (a) Frequency distributions from individual Technora® scans, as well as total distribution across all scans (thick red line). (b) Corresponding individual distributions and total distribution from K29. (c) Comparison between total frequency distributions. Solid vertical lines denote mean bulk values reported from published microscale experiments [8,19].

sudden topographical jumps up to tens of nanometers. This indicates that, when the fiber is separated after FIB notching, the crack that forms the exposed surface follows these interfaces rather than fracturing crystallites within the fibrils. In contrast, the exposed plane within Technora® is significantly flatter and less well-defined, as evidenced by surface fibrils penetrating into and out of the exposed surface. Without forming crystallites in the lateral direction, there appears to be a lack of consistent lateral packing in Technora®; thus, the fiber cannot break along well-defined planes. This explains how the complex nanostructure translates up to the microstructure, leading to more disorder in 3D space in Technora® compared to Kevlar®.

The other unique microstructural aspect is the lack of a fiber skin in our real-space AFM scans of Technora®. In Kevlar®, the skin is a prominent feature up to ca. 1 μm thick and readily observable with AFM and other techniques [11,13,16,20,21]. It is expected to arise during Kevlar® fiber processing due to different cooling rates near the surface of the fiber and inside the fiber; consequently, Kevlar® fibers that undergo post-processing heat treatments possess thinner skins [11,13,15]. In previous studies, we corroborated this trend for different classes of Kevlar® fibers using real-space AFM scans, as skin regions contained distinct topographical features and lower stiffness than the Kevlar® fiber core [11,13]. For Technora®, however, no such features were ever observed. There are shallow topographical gradations near the outer edges of the fiber (Figure 2c), but these are distinct from the sharp changes at the skin–core interface we observed in Kevlar®. Moreover, there are no clear stiffness variations near the periphery compared to the fiber center, suggesting no change in the underlying material structure across the fiber diameter. We expect that this lack of a skin–core structure is yet another manifestation of the non-crystalline structure within Technora®, resulting in an ostensibly homogeneous microstructure throughout the fiber.

Transverse elastic modulus quantifications

We begin our discussion of the transverse elastic modulus measurements by focusing on the distributions in E_T values (i) within each fiber type and (ii) between the two fiber classes. Both means and modes are important statistical averages to consider in the context of these experiments. The mean provides an overall average mechanical response, but it is more sensitive to impacts of individual scans than the mode, which tells us the E_T value measured most frequently in different areas. For example, in the overall E_T distribution in Technora® (Figure 8a), the highest peak (i.e., the mode) is centered at 1.53 GPa, while secondary peaks and shoulders in the distribution arise at other values, for example, at ca. 2.6 GPa and, less prominently, around 0.5 GPa. Yet for Technora®, it is interesting to note that multiple individual peaks center around the mode of 1.53 GPa. While the Kevlar® K29 mean E_T is only 9% higher than that of Technora®, the shapes of the individual and total distributions resembled plateaus with shallow peaks. Technically, the mode of the K29 measurements is 2.79 GPa, but another shallow peak in the plateau centered appears at 1.1 GPa.

In contrast to the modulus maps in Technora®, the distinctions between the local E_T measurements within fibrils and their interfaces are very clear in Kevlar®. Image thresholding of K29 modulus maps indicates that the most compliant regions are near interfaces, which can also be readily observed from lateral line scans (Figure 7c). However, these interfaces are not uniformly compliant, that is, different interfaces exhibit unique

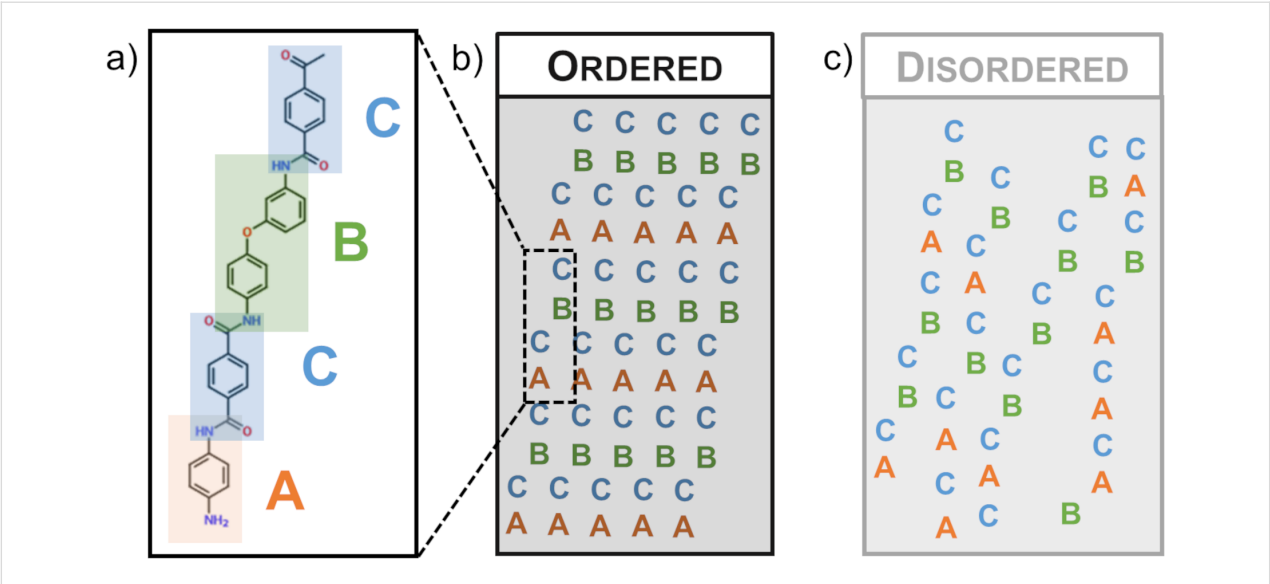

Figure 9: Schematic of possible molecular sequencing in Technora® fibers. (a) With random sequences of molecular subunits (e.g., ACBC, top left), adjacent extended chain molecules can form ordered or disordered subdomains, per theoretical schematics highlighted in (b) and (c). Fibrils directly observed in this study suggest that even some disordered subdomains can have sufficiently strong interactions to form fibrils.

E_T values. Each one is consistent along the fiber axis (i.e., the stiffness along any particular interface is uniform), but they are not consistent with one another. This compliance likely stems from a local reduction in contact area, as sudden changes in height up to tens of nanometers can occur at these interfaces (Figure 7a). Nevertheless, these are "real" E_T values; in other words, these local gaps in the fiber would affect E_T of the full fiber. Individual Kevlar® fibrils typically exhibit their highest E_T values toward their centers; however, the modulus values among fibrils vary. The apparently independent values of fibrils and their interfaces can explain the overall plateau-like distribution of E_T in Kevlar®. In addition, the fundamental chemistry of Kevlar® (Figure 1) leads to a well-ordered molecular structure (i.e., 'ACACAC…' in Figure 9), which should enhance load transfer at this scale compared to Technora®. Together, the more uniform molecular sequencing and the resulting microstructure in Kevlar® appear to explain why K29 has higher mean and mode E_T values than Technora® in our measurements.

Finally, it is important to compare our nanoscale AFM measurements of transverse moduli with full-fiber transverse compression experiments conducted in other studies. We find that the modes from our AFM-based measurements correspond closely with the full-fiber E_T values from two different studies [8,19]. For Technora®, remarkably similar quantitative values (AFM: 1.53 GPa; mean full-fiber: 1.64 GPa) may reflect how the microstructure throughout the fiber (Figure 2) consistently reflects the nanostructure (Figure 4). Thus, we would expect the E_T measurements to be similar across length scales.

The analysis for Kevlar®, however, is more complicated. Our nanoscale E_T measurements indicate stiffer average mechanical responses in Kevlar® K29 than in Technora®, in agreement with the aforementioned full-fiber experiments [8,19]. However, we must acknowledge the plateau-like nature of the distribution in our measurements, with a second peak near 1.1 GPa. Moreover, at the full-fiber level, the skin–core structure in Kevlar® must be considered. Previous studies have suggested that Kevlar® skins are more compliant than the cores [11,13,20,21]. We have implicitly focused on Kevlar® cores, but when full Kevlar® fibers are subjected to transverse compression, we would expect a mixed mechanical response based on both core and skin stiffness. Thus, our broad distributions in nanoscale Kevlar® values and this clear distinction between nano- and microstructural characterization of Kevlar® make this comparison less conclusive than that of Technora®. Nevertheless, the fact that these materials exhibit similar transverse elastic responses at the nanoscale and across the full fiber is noteworthy, and appears to support the validity of quantitative materials characterization at the nanoscale with this technique.

Technora® vs Kevlar® K29: structure–property connections

Tensile properties

The structural distinctions between Technora® and Kevlar® K29 have fascinating implications for the tensile mechanical properties of these fiber classes. Studies have shown that their mean single-fiber tensile properties, for example, tensile strength and elastic modulus, are quite similar [6,7]. In addition,

Technora® single-fiber tensile strengths are more consistent than those of Kevlar® K29 [6,7]. The similar mean tensile properties appear to support the hypothesis put forth by Ozawa, that is, a well-defined crystal structure is not required for a high-performance polymer fiber, provided that fixing extended-chain molecules and aligning them with the fiber axis can be achieved through other means [1]. Indeed, the tensile strengths of high-performance paracrystalline fibers are nearly an order of magnitude lower than those of their constituent molecules and crystallites, so other structural factors play a considerable role in limiting fiber properties [22]. To this end, the more consistent strength values of Technora® appear to stem from two sources. First, as noted by Morgan et al., a paracrystalline fiber such as Kevlar® will have preferential fracture planes across its core, in agreement with AFM profiles shown here (Figure 7c) that clearly demarcate a fracture path between fibrils [15]. When a crack extends into the fiber core, the failure will be brittle and thus more prone to variation. In contrast, Technora® has no such preferential planes, which may explain its more consistent strength values [6,7]. Indeed, we observe stray fibrils protruding in and out of the FIB-notched surfaces of Technora® and no consistent fracture planes (Figure 7c), which would necessitate fibrils breaking or separating in a manner inconsistent with brittle failure.

Second, the presence or absence of skin–core differentiation likely plays a critical role in dictating the distributions of the tensile strengths of these fibers as well. Şahin et al. suggest that the skin–core interface dominates the ultimate tensile strength of Kevlar®, as evidenced by a "sword-in-sheath" pullout of the core from the skin during tensile tests [23]. Kevlar® fibers with larger skins typically exhibit higher tensile strength as well, suggesting that the load-bearing capabilities of these fibers are significantly diminished once a crack permeates the skin [11,13,16]. This interface appears to be another mechanism that leads to a somewhat brittle failure in Kevlar®, resulting in a distribution in single-fiber tensile strengths. In contrast, the lack of skin–core differentiation in Technora®, evidenced here via real-space scans, should also lead to more consistent strength values.

Additional mechanical properties

Significant connections can also be made between the structures of Technora® and Kevlar® fibers and other mechanical properties, such as creep and fatigue. Ferreira et al. demonstrated that, while neither Technora® nor Kevlar® fibers exhibit significant amounts of creep deformation, Technora® fibers creep slightly less [6]. They hypothesized that this distribution stems from more local links between adjacent molecular chains in Technora® than between crystallites in Kevlar® [6]. Extending this molecular-level hypothesis, it is likely that the highly fibrillated nanostructure in Technora® (Figure 3 and Figure 4) has the same effect. Local, randomly distributed load transfers between fibrils could more effectively inhibit creep at this length scale than highly aligned fibrils such as those in Kevlar®. Creep behavior could also be affected considerably by the microstructures of the fibers. In Kevlar®, the well-defined pleated microstructure would be prone to deform under creep, while the heterogeneous Technora® microstructure would be less likely to deform in a consistent manner throughout the fiber [24].

These structure–property connections appear to correlate with the fatigue behavior of these fibers as well. Ferreira et al. found that Technora® fibers exhibited the same tensile moduli through 80 load cycles, while Kevlar® K29 fiber moduli changed several times under cyclic loading [6]. Most notably, after 20 cycles, a new regime of lower tensile modulus under high loads was observed in Kevlar®, which the authors attributed to interfaces between PPTA crystallites breaking irreversibly [6]. Ozawa also found that Technora® was more resistant to fatigue than Kevlar® and attributed this difference to two fundamental molecular mechanisms: the more compliant molecular chain and the "less developed" crystal structures in Technora® [1]. These molecular-level features likely explain the nanoscale features in our AFM maps, as discussed earlier. In turn, it appears that this heterogeneous structure makes Technora® fibers less prone to both creep and fatigue than Kevlar®.

Multifunctional properties

Beyond establishing connections between fiber structures and mechanical properties of Technora® and Kevlar®, it is also important to highlight how structural features relate to multifunctional properties. One such property is resistance to chemical attacks. By measuring the tenacity (i.e., tensile strength) of Kevlar® K29 and Technora® fibers immersed in both basic and acidic solutions, Ozawa found that Technora® fibers are typically an order of magnitude more resistant to chemical attacks than Kevlar® K29 [1]. A small but important subset of ambient "chemical" attacks includes moisture sensitivity. Ozawa observed substantially larger tenacity reductions in Kevlar® than in Technora® as a function of ambient moisture [1]. Minoshima et al. also found that Kevlar® K29 fibers absorbed about 6.6 times more deionized water than Technora® when immersed, which resulted in larger reductions in full-fiber E_T for Kevlar® [8]. These findings appear to reflect the distinct fiber microstructures. In Kevlar®, the well-defined pleated sheet structure allows for preferential planes through which intercalating chemicals can permeate and interact with the material [1,15]. This is particularly true for the interfaces we observe between fibrils, where needle-like voids can coalesce and create ideal planes for chemical infiltration [25]. In contrast, the branched filaments within Technora® fibers present no such

consistent internal planes. Indeed, Ozawa hypothesized that Kevlar® has much wider "internal surfaces" than Technora®, making the former more sensitive to chemical effects [1]. This hypothesis aligns very well with our line scans (Figure 6), which show Kevlar® exhibiting longer and more clearly defined interfaces than Technora®. Thus, through real-space AFM measurements, we have expanded upon previous hypotheses by uncovering how these internal morphological features take shape, helping to explain how structures affect fiber properties.

Conclusion

Here we present internal structural characterizations of FIB-notched Technora® fibers using multifrequency AFM mapping. We observe a homogeneous microstructure throughout the fiber without any evidence of a fiber skin near the periphery. At the nanoscale, we observe a highly fibrillated structure well aligned with the fiber axis with significant fibril branching, junctions, and weaving in and out of the exposed surface. Combining topography maps with stiffness maps, we find that locally elevated regions exhibit higher stiffness, regardless of scanning direction, orientation with the fiber axis, or the relative heights of different sections (e.g., single fibrils versus nodes between multiple fibrils).

Our nano- and microscale characterizations of Technora® are further aided by extensive comparisons with Kevlar® K29, which possesses similar mechanical properties despite a significantly different internal structure. Comparisons of AFM maps from each fiber class revealed that the Technora® nanostructure includes (i) more fibril branching, (ii) less-defined interfaces, and (iii) more homogeneous stiffness profiles than in Kevlar® K29. These semiquantitive comparisons of stiffness were further supported by direct quantification of transverse elastic modulus (E_T) of both fiber types, which showed more consistent E_T measurements in Technora® than in Kevlar® K29. Nanoscale E_T measurements in Technora® also matched exceptionally well with previously reported macroscopic measurements, which would be expected for a homogeneous microstructure. In contrast, our nanoscale measurements did not match as well with macroscopic measurements of Kevlar® K29, perhaps as a result of the skin–core structure present in Kevlar® K29 but absent in Technora®.

Taken together, our characterizations uncover the internal structures of these fiber classes, which in turn help explain the mechanical and multifunctional performances of these fiber classes reported in other studies. In the future it would be especially interesting to carry out higher resolution scans within these fibers to characterize atomic structure [26]. Flat Technora® subdomains may be especially amenable to this characterization, which could shed more light on the sequencing of molecular subdomains (Figure 9) discussed here and in previous reports [2-5]. In addition, it would be interesting to apply the FIB notch technique to Kevlar® and Technora® fibers that underwent mechanical conditioning (e.g., fatigue) and/or chemical treatment to complement prior characterizations and improve our understanding of the mechanisms that determine the multifunctional performance of these fibers.

Experimental

Materials

Individual Technora® T-240 fibers were extracted from a 65 decitex yarn. Fibers were mounted onto cardstock specimen holders, fixed with adhesive at two points approximately 15 mm apart from one another, and conductively coated with a gold–palladium mixture to mitigate sample drift, for example, due to sample charging effects inside the FIB chamber [9]. Kevlar® K29 fibers also discussed in this report underwent the same preparation techniques.

Focused ion beam notching

Conductively coated fibers were cut with a FIB as discussed in detail in an earlier study [9]. In summary, 2–3 μm wide through-cuts were notched into each fiber (Figure 1b), extending halfway up or down the fiber diameter on opposing ends. This creates a shear plane that readily splits the fiber under slight tension, exposing internal surfaces that can be probed with AFM. Notches were obtained using a gallium ion beam inside an FEI NanoV600 dual beam system, with ion beam voltage and current of 16 kV and 3.3 nA, respectively. After FIB notching, specimens were mounted onto magnetic discs with double-sided tape as shown (Figure 1c) for AFM characterization [9].

The internal fiber surfaces produced by FIB notching closely match corresponding surfaces obtained using other techniques, as previous studies have shown for Kevlar® [9,11,14]. While microtomy can also be used to access internal fiber surfaces, marks from the microtome blade often remain visible [9], which is a disadvantage compared to FIB-notched surfaces. However, each FIB notch must be carefully prepared so that it laterally cuts through half of the diameter, or slightly more. Undercutting prevents a shear plane from forming, yielding a highly fibrillated internal surface that cannot be characterized with AFM, as stray fibrils protrude from the surface and move when contacted by the tip. In contrast, overcutting leads to transverse failures near the notches without producing an internal shear plane.

Multifrequency atomic force microscopy scanning

The exposed internal surfaces of FIB-notched fibers were scanned using a Cypher AFM with an ARC2 controller

(Asylum Research). Olympus AC200TS cantilevers ($k \approx 9$ N/m (nominal), k = 12–21 N/m (measured)) were used for AFM scans. By simultaneously exciting the AFM cantilever to its first and second resonance (f_1 = 160–190 kHz and f_2 = 900–1150 kHz, Figure 1c) and applying two distinct control conditions (amplitude modulation (AM) and frequency modulation (FM) to the first and second modes, respectively), maps of surface topography, transverse stiffness, and transverse elastic modulus across the fiber were obtained. Typical (setpoint/free air) amplitudes for the first mode were ca. 25/50 nm. Second mode amplitudes (always held constant, in and out of contact) were approximately 1–2 nm. Some images were enhanced by approximately doubling both the setpoint and free air amplitudes while maintaining the amplitude ratio close to 50%. Typical map sizes and resolutions ranged from 500 nm × 500 nm (512 × 512 pixels, ca. 1 nm/pixel) to 20 × 20 μm (2048 × 2048 pixels, ca. 10 nm/pixel), depending on whether the map was intended to characterize fiber nanostructure or microstructure.

To clarify, both transverse stiffness and transverse elastic modulus maps obtained with AFM provide information about the local mechanical response of the material. Transverse stiffness (or "stiffness"), quantified in [N/m], makes no assumptions about tip–substrate interactions such as tip size or shape. It is primarily useful for semi-quantitative mapping to show the relative fluctuations in stiffness within different regions. However, stiffness itself is not a material property, that is, using AFM tips with different shapes and sizes, or worn tips, will yield different stiffness values. Thus, when presenting transverse stiffness values, we focus on the relative variations within different maps.

Maps of transverse elastic modulus (E_T), quantified in [GPa], directly quantify nanoscale material properties of the fiber surface, though they present additional challenges versus stiffness maps that must be addressed. In particular, tip wear has to be carefully monitored to ensure that the tip radius is well characterized in each scan. Here we focused E_T analysis on small fiber subdomains (typically 500 nm × 500 nm, ca. 1 nm/pixel) to reduce the likelihood of tip wear. In addition, subdomains were initially mapped out with "sacrificial" AFM tips, and E_T distributions were only then obtained from scans with fresh, well-characterized AFM tips. In quantitative scans, the shape of each AFM tip was taken to be a cylindrical punch, and the tip radius was calibrated by scanning on polystyrene ($E_{T,PS}$ = 2.7 GPa, Bruker) as a control substrate before and after each scan on a fiber surface. E_T quantifications from fiber maps were only kept when mean $E_{T,PS}$ values varied by less than 10% between the pre- and post-scans on polystyrene.

To ensure repeatability of measurements and observations, AFM maps and quantitative data were each obtained from at least one region in two separate Technora® and two separate Kevlar® fibers. The E_T measurements were the most restrictive considering the need for pre- and post-scans to confirm calibration. Additional scans were obtained from other regions within the same fibers, as well as other fibers, and we observed similar features to those reported here. For clarity, our analysis has focused on regions that were most clearly defined in AFM scans.

Line profiles, E_T distributions, and other quantifications of AFM maps were characterized using the Gwyddion software package [27]. Additional details on multifrequency AFM mapping theory, analysis and applications have been provided in earlier literature reports [10,28,29].

Acknowledgements

Technora® T-240 fibers were provided by NSRDEC in Natick, MA, USA. Kevlar® K29 fibers were provided by DuPont™. The authors acknowledge Mehdi Afshari, Jim Singletary, Emil Sandoz-Rosado, Eric Wetzel, and Steve Lustig for helpful discussions. The views expressed in this paper are those of the authors and do not necessarily represent the views of the U.S. Merchant Marine Academy, Maritime Administration, the U.S. Department of Transportation, the U.S. Army Research Lab, the U.S. Department of Defense, or the United States.

Funding

This research was supported in part by an appointment to the Postgraduate Research Participation Program at the U.S. Army Research Laboratory administered by the Oak Ridge Institute for Science and Education (Contract ORISE 1120-1120-99) through an interagency agreement between the U.S. Department of Energy and USARL.

ORCID® iDs

Michael R. Roenbeck - https://orcid.org/0000-0003-3446-6653
Kenneth E. Strawhecker - https://orcid.org/0000-0002-3462-4757

References

1. Ozawa, S. *Polym. J.* **1987,** *19,* 119–125. doi:10.1295/polymj.19.119
2. Blackwell, J.; Cageao, R. A.; Biswas, A. *Macromolecules* **1987,** *20,* 667–671. doi:10.1021/ma00169a033
3. Wu, T.-M.; Blackwell, J. *Macromolecules* **1996,** *29,* 5621–5627. doi:10.1021/ma951426e
4. Wu, T.-M.; Blackwell, J. *J. Polym. Res.* **1997,** *4,* 25–32. doi:10.1007/s10965-006-0004-4
5. Matsuda, H.; Asakura, T.; Nakagawa, Y. *Macromolecules* **2003,** *36,* 6160–6165. doi:10.1021/ma034670b
6. Ferreira, M.; Lam, T. M.; Labache, P.; Delvael, Y. *Text. Res. J.* **1999,** *69,* 30–37. doi:10.1177/004051759906900106

7. Naito, K. *J. Appl. Polym. Sci.* **2013,** *128,* 1185–1192. doi:10.1002/app.38420
8. Minoshima, K.; Maekawa, Y.; Yamada, T.; Komai, K. *JSME Int. J., Ser. A* **2000,** *43,* 69–75. doi:10.1299/jsmea.43.69
9. Stockdale, T. A.; Strawhecker, K. E.; Sandoz-Rosado, E. J.; Wetzel, E. D. *Mater. Lett.* **2016,** *176,* 173–176. doi:10.1016/j.matlet.2016.04.082
10. Strawhecker, K. E.; Sandoz-Rosado, E. J.; Stockdale, T. A.; Laird, E. D. *Polymer* **2016,** *103,* 224–232. doi:10.1016/j.polymer.2016.09.062
11. Roenbeck, M. R.; Sandoz-Rosado, E. J.; Cline, J.; Wu, V.; Moy, P.; Afshari, M.; Reichert, D.; Lustig, S. R.; Strawhecker, K. E. *Polymer* **2017,** *128,* 200–210. doi:10.1016/j.polymer.2017.09.039
12. Sandoz-Rosado, E.; Roenbeck, M. R.; Strawhecker, K. E. *Scanning* **2018,** 1–12. doi:10.1155/2018/4975317
13. Roenbeck, M. R.; Cline, J.; Wu, V.; Afshari, M.; Kellner, S.; Martin, P.; Londono, J. D.; Clinger, L. E.; Reichert, D.; Lustig, S. R.; Strawhecker, K. E. *J. Mater. Sci.* **2019,** *54,* 6668–6683. doi:10.1007/s10853-018-03282-x
14. Dobb, M. G.; Johnson, D. J.; Saville, B. P. *J. Polym. Sci., Polym. Phys. Ed.* **1977,** *15,* 2201–2211. doi:10.1002/pol.1977.180151212
15. Morgan, R. J.; Pruneda, C. O.; Steele, W. J. *J. Polym. Sci., Polym. Phys. Ed.* **1983,** *21,* 1757–1783. doi:10.1002/pol.1983.180210913
16. Dobb, M. G.; Robson, R. M. *J. Mater. Sci.* **1990,** *25,* 459–464. doi:10.1007/bf00714056
17. Derombise, G.; Vouyovitch Van Schoors, L.; Davies, P. *Polym. Degrad. Stab.* **2009,** *94,* 1615–1620. doi:10.1016/j.polymdegradstab.2009.07.021
18. Sawyer, L. C.; Chen, R. T.; Jamieson, M. G.; Musselman, I. H.; Russell, P. E. *J. Mater. Sci.* **1993,** *28,* 225–238. doi:10.1007/bf00349055
19. Kitagawa, T.; Ishitobi, M.; Yabuki, K. *J. Polym. Sci., Part B: Polym. Phys.* **2000,** *38,* 1605–1611. doi:10.1002/(sici)1099-0488(20000615)38:12<1605::aid-polb50>3.0.co;2-z
20. Graham, J. F.; McCague, C.; Warren, O. L.; Norton, P. R. *Polymer* **2000,** *41,* 4761–4764. doi:10.1016/s0032-3861(99)00661-8
21. McAllister, Q. P.; Gillespie, J. W., Jr.; VanLandingham, M. R. *J. Mater. Res.* **2012,** *27,* 1824–1837. doi:10.1557/jmr.2012.80
22. Crist, B. *Annu. Rev. Mater. Sci.* **1995,** *25,* 295–323. doi:10.1146/annurev.ms.25.080195.001455
23. Şahin, K.; Clawson, J. K.; Singletary, J.; Horner, S.; Zheng, J.; Pelegri, A.; Chasiotis, I. *Polymer* **2018,** *140,* 96–106. doi:10.1016/j.polymer.2018.02.018
24. Ericksen, R. H. *Polymer* **1985,** *26,* 733–746. doi:10.1016/0032-3861(85)90111-9
25. Dobb, M. G.; Johnson, D. J.; Majeed, A.; Saville, B. P. *Polymer* **1979,** *20,* 1284–1288. doi:10.1016/0032-3861(79)90157-5
26. Garcia, R. *Chem. Soc. Rev.* **2020,** *49,* 5850–5884. doi:10.1039/d0cs00318b
27. Nečas, D.; Klapetek, P. *Cent. Eur. J. Phys.* **2012,** *10,* 181–188. doi:10.2478/s11534-011-0096-2
28. Labuda, A.; Kocuń, M.; Meinhold, W.; Walters, D.; Proksch, R. *Beilstein J. Nanotechnol.* **2016,** *7,* 970–982. doi:10.3762/bjnano.7.89
29. Benaglia, S.; Gisbert, V. G.; Perrino, A. P.; Amo, C. A.; Garcia, R. *Nat. Protoc.* **2018,** *13,* 2890–2907. doi:10.1038/s41596-018-0070-1

License and Terms

BEILSTEIN JOURNAL OF NANOTECHNOLOGY

TEM sample preparation of lithographically patterned permalloy nanostructures on silicon nitride membranes

Joshua Williams*[1,2], Michael I. Faley*[1], Joseph Vimal Vas[1], Peng-Han Lu[1] and Rafal E. Dunin-Borkowski[1]

Full Research Paper

Open Access

Address:
[1]Ernst Ruska-Centre for Microscopy and Spectroscopy with Electrons, Forschungszentrum Jülich, 52425 Jülich, Germany and [2]Faculty of Engineering, University Duisburg-Essen, 47057 Duisburg, Germany

Email:
Joshua Williams* - j.williams@fz-juelich.de; Michael I. Faley* - m.faley@fz-juelich.de

* Corresponding author

Keywords:
electron holography; Lorentz transmission electron microscopy; magnetic imaging; nanodisk; nanofabrication; permalloy

Beilstein J. Nanotechnol. **2024,** *15,* 1–12.
https://doi.org/10.3762/bjnano.15.1

Received: 31 August 2023
Accepted: 28 November 2023
Published: 02 January 2024

This article is part of the thematic issue "Correlative approaches in materials science – from the micrometer to the nanometer scale".

Associate Editor: A. Gölzhäuser

Abstract

We have prepared ferromagnetic nanostructures intended for the investigation of high-frequency magnetization dynamics in permalloy (Py) nanodisks using Lorentz transmission electron microscopy (LTEM) and electron holography. Py nanodisks were fabricated on thin silicon nitride (SiN) membranes using three different fabrication methods: lift-off, ion beam etching (IBE), and stencil lithography. They were further analyzed using different instruments, including scanning electron microscopy, LTEM, and electron holography. A bilayer of positive PMMA resist was utilized in the first fabrication method to form an undercut structure that guarantees a clean lift-off procedure. The second approach used dry etching with an Ar beam to etch a thin Py film, while an electron-beam-patterned negative resist mask kept the desired structure. In the third process, nanostencils (shadow masks) with submicrometer apertures were milled on SiN membranes using a focused ion beam. Furthermore, we have developed a new TEM sample preparation method, where we fabricated Py nanostructures on a bulk substrate with a SiN buffer layer and etched the substrate to create a thin SiN membrane under the Py nanostructure. Finally, we observed the vortex dynamics of the Py nanodisk under magnetic fields using LTEM and off-axis electron holography. A correlation between preparation methods and the properties of the Py nanostructures was made.

Introduction

The ability to study the spatial distribution of magnetization in ferromagnetic nanostructures is important for developing nanoelectronics, particularly for data storage and information processing. A vortex spin configuration has been observed in Py nanodisks [1,2] with independent polarity and helicity [3]. Since then, many studies have been done on manipulating magnetic

vortices inside Py nanodisks using micromagnetic simulations [4-6] and a variety of magnetic measurement techniques including magnetic force microscopy [7], transmission electron microscopy (TEM) [1,8-11], scanning transmission X-ray microscopy [12,13], and magneto-optical Kerr effect microscopy [14,15]. Possible applications of Py nanodisks were proposed for zero-hysteresis magnet sensors, magnetic logic devices, and data storage [16]. Py is a nickel–iron alloy (80 atom % Ni and 20 atom % Fe) that has a small coercive field (H_c) [17] and low magnetostriction (λ_s) [18], as well as high permeability and high saturation magnetization (M_s) [19].

TEM offers high spatial resolution for magnetic imaging. TEM-based magnetic imaging techniques such as Lorentz microscopy and electron holography, along with simultaneous structural and chemical characterization techniques such as electron diffraction, 4D STEM, and energy-dispersive X-ray (EDX) and electron energy loss spectroscopy (EELS), enable a correlative characterization to investigate magnetic information down to the nanometer/atomic scale. However, the corresponding samples need to be prepared on electron-beam-transparent membranes, which are very fragile and can easily break during standard lithography procedures. Although a lift-off approach has been demonstrated [20], alternative methods may be advantageous in terms of structural resolution, process simplicity, and the absence of resist residues [21]. We have fabricated ferromagnetic nanodisks on a conventional TEM grid from TedPella® using three different fabrication methods.

In the first method, a bilayer of positive PMMA resist yielded an undercut structure. The resist was patterned using an electron beam, which offers higher resolution than other sources (e.g., UV light) because of the smaller wavelength of electrons. Since the use of an ultrasonic bath will destroy the free-standing membrane, the undercut must be deliberately made larger to ensure a clean lift-off process. The larger undercut is realized by multi-dose exposure, which consists of two parts: The main exposure is for patterning the nominal structure, and an additional exposure is for patterning the outline of the nominal structure. This additional exposure is performed with a lower dose than the main exposure so that it does not induce chain scission in the top resist layer, but only in the bottom resist layer, which is more sensitive. The result of the multi-dose exposure was controlled by observing a cross section of the developed bilayer resist using a SEM in snapshot mode to avoid melting of the PMMA resist. The second approach involved etching a thin Py film with an ion beam while preserving the intended structure with an electron-beam-patterned negative resist mask. Redeposition of etched material was found to construct fences at the edges of the structures. Fences and edge roughness from the imperfect lift-off process were reported to influence the magnetic properties of nanostructures [22]. The third method, stencil lithography, makes use of a shadow mask, which was fabricated by milling submicrometer apertures on a conventional TEM grid using a focused ion beam. This method avoids the resist-based fabrication, which is common in preparing nanodisk samples for TEM [8,20].

We have also developed a method of sample preparation for patterned nanostructures starting from a bulk substrate. This method is versatile and might be useful for more complicated lithographically patterned nanostructures to be examined using TEM. The results of the fabrication methods mentioned above were examined using SEM. This is important because the structural information (disk dimensions and deformation from fences) later correlates to the magnetic properties. A magnetic vortex configuration occurs only under the right diameter/thickness ratio, otherwise either a single or multiple magnetic domains will appear.

After Py nanodots of various sizes were fabricated, we used Lorentz transmission electron microscopy (LTEM) and off-axis electron holography to study their magnetic domain structure. The microscope is operated in a magnetic-field-free mode. In this case, the objective lens is turned off, and the Lorentz lens is used instead to focus the electron beam onto the back focal plane. As the electron beam passes through the sample, the in-plane sample magnetization exerts a Lorentz force onto the electron beam, which deflects the beam. The force on each electron in the beam is given by

$$F = -e\left(v \times B\right), \tag{1}$$

where F is the force, e is the charge, v is the relativistic velocity of the electron beam, and B is the magnetic field exerted by the sample.

In the case of a vortex structure, the electron beam is deflected by the circularly oriented magnetic fields. The magnetic contrast can hardly be observed when the image is in-focus but becomes more visible when the image is defocused. On one side of the focus, the magnetization of the vortex deflects the electron beams inwards, which then overlaps and results in a white contrast in the center. On the other side of the focus, the beam will be deflected outwards leaving an empty area and, therefore, a dark contrast in the center [23].

Off-axis electron holography is obtained from the interference (holograms) of the electron wave modulated by the magnetic sample and a coherently tilted reference plane wave. The intensity of the hologram can be represented in the form of

$$I_{\mathrm{hol}}(\mathbf{r}) = \left|\Psi_{\mathrm{i}}(\mathbf{r}) + \exp\left[2\pi \mathrm{i}\ \mathbf{q}\cdot\mathbf{r}\right]\right|^2 = 1 + A_{\mathrm{i}}^2(\mathbf{r}) + 2A_{\mathrm{i}}(\mathbf{r})\cos\left[2\pi \mathrm{i}\ \mathbf{q}\cdot\mathbf{r} + \varphi_{\mathrm{i}}(\mathbf{r})\right], \quad (2)$$

where $\Psi_{\mathrm{i}}(\mathbf{r})$ stands for the electron wavefunction in the image plane i with amplitude A_{i} and phase φ_{i}, $\mathbf{r}$ is a two-dimensional vector in the sample plane, and $\mathbf{q}$ is the two-dimensional reciprocal space vector related to the tilt of the reference wave. Note that the phase $\varphi_{\mathrm{i}}(\mathbf{r})$ is now separated in the third term inside the cosine; it can be retrieved by taking the fast Fourier transform (FFT) of the intensity [24]. The phase shift can then be used to recover the in-plane magnetic information inside the sample.

Results and Discussion

Fabrication on a commercial SiN membrane

Lift-off

The lift-off procedure is described in Figure 1. We use PMMA and its copolymer as a positive resist to create a bilayer resist. The copolymer (AR-P 617.08) is a methyl methacrylate and methacrylic acid copolymer dissolved in 1-methoxy-2-propanol with a solid content of 8%. Its viscosity is 36 mPa·s. After spinning at 4000 rpm and baking at 200 °C for 25 min, it has a thickness of around 500 nm. To spin coat a 3 mm TEM grid (Figure 2a,b), we used a special adapter (Figure 2c). The high baking temperature and the relatively long baking duration were chosen because the copolymer must be solid to prevent dissolution by the PMMA layer. In addition, the baking temperature can control the sensitivity of the copolymer. The higher the baking temperature of the copolymer, the more sensitive the copolymer gets. This is because more anhydride 6-rings form, which break apart more easily than the aliphatic chain remainder during electron beam exposure [25]. AR-P 679.04 is polymethylmethacrylate (PMMA) dissolved in ethyl lactate with a solid content of 4%. Its molecular weight is 950,000, and it has a high resolution as well as a low sensitivity. Its viscosity is 16.4 mPa·s. After spinning at 4000 rpm and baking at 180 °C for 5 min, it has a thickness of around 300 nm. The exposure is carried out using an electron beam lithography system Vistec EBPG 5000+ operating at 100 kV. Working on a thin transparent membrane also allows for high-resolution patterning since there is less electron scattering during exposure [26].

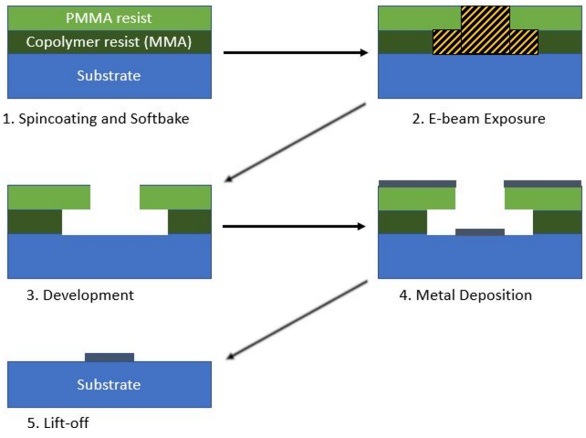

Figure 1: Lift-off fabrication process.

The purpose of applying two layers of resist is to create a large undercut by using a bottom layer that is more sensitive than the top layer. This prevents the unwanted deposition of metal that sticks to the side of the resist after lift-off. A larger undercut was achieved on multilayer resist with the help of multiple exposures [27]. The idea is to expose the resist layer by layer: The bottom resist was deposited and exposed. Then, aluminium was deposited as a spacer between the bottom and top layer to prevent the top layer from dissolving the lower one. Next, the

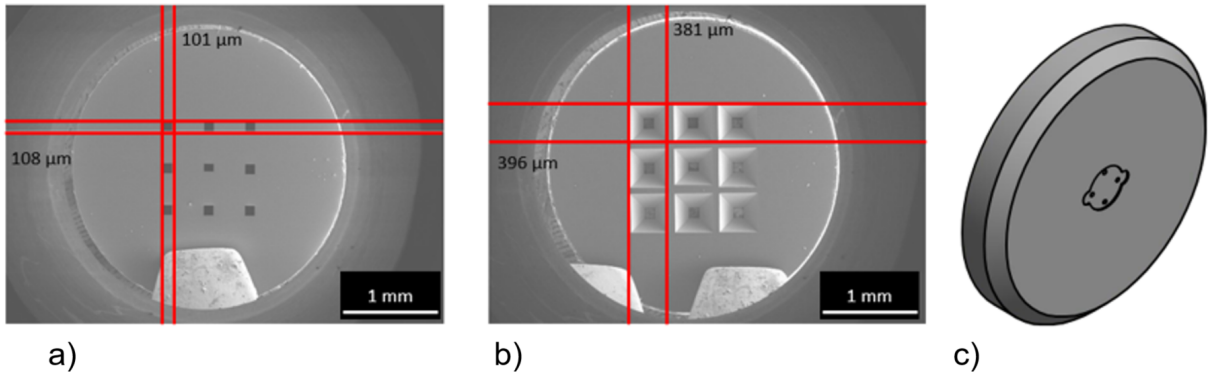

Figure 2: SEM images of the 3 mm TEM window grid that provides nine windows of free-standing 50 nm thick SiN membrane. (a) Front side and (b) back side. (c) Spin coating adapter for the 3 mm TEM grid.

top resist layer was deposited and exposed to the nominal size. The structure was developed from top to bottom including removal of the Al spacer. The development of the bottom layer, in other words the size of the undercut, is controlled only by the development time. In a more recent study, the Al spacer was omitted, and the development was done with one solution since the bilayer resist is made from PMMA and its copolymer [28]. The process is quite time-consuming since the exposures are done layer by layer.

Considering the two techniques, a one-time exposure is possible with the help of high accelerating voltage during electron beam exposure. In this process, rather than doing one resist deposition and exposure after another, the layer selectivity is controlled by the electron beam dose and the sensitivity of the two layers. Only in the copolymer (higher sensitivity) the chain scission reaction occurs at low doses; at higher doses, both layers were exposed. The exposure scheme is given in Figure 3.

The doses were chosen by considering that the copolymer is 2–3 times more sensitive than PMMA [25]. If the exposure dose is too small, then the undercut will not develop; if it is too high, then PMMA will dissolve in a larger area than the nominal diameter. It takes approximately 15 min development time to get 2 µm undercut that is shown in Figure 3b.

Once the resist was developed, we deposited a 50 nm thick layer of Py using magnetron sputtering through the resist aperture. We used DC magnetron sputtering in a pure Ar environment at a pressure of 1 Pa to deposit Py at room temperature. The effective permalloy target had a diameter of 8 mm. The sputtered material almost forms a parallel beam when it approaches the substrate at a target–substrate distance of around 8 cm. The sputtered film was investigated under HRTEM. It was revealed that the film is polycrystalline with a lattice spacing of 0.36 nm (Figure 4), which correlates to the lattice constant of Py.

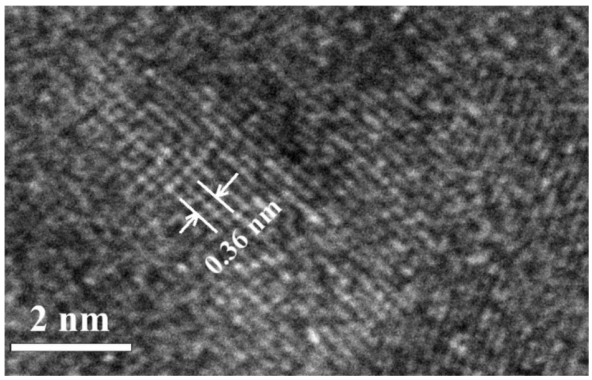

Figure 4: HRTEM image of a Py nanodisk. The grain sizes are around 6 nm.

The lift-off technique allows for the fabrication of arrays of 220 nm disks spaced 80 nm apart (see Figure 5c). With the help of the undercut, there is significantly less debris of metal after lift-off (Figure 5a). In comparison, the arrows on the lower part of Figure 5d demonstrate the lift-off result without a big undercut, which leads to fences of Py deposited on the sides of the resist. There are, however, a few limitations to consider: The spin-coated resist may be inhomogeneous (edge bead effect) on smaller substrates, reducing the region where high-quality structures may be obtained. Furthermore, one cannot deposit metals at high temperature, and one has to establish a good thermal contact during metal deposition to prevent the resist mask from melting as the substrate temperature is above the glass transition temperature of the resist.

Ion beam etching

The IBE process (Figure 6) is as follows: The first step is to deposit Py on the substrate; then a negative resist is spin-coated on top. The resist used is AZ® nLof 2020 diluted with AZ® EBR solvent. The producers describe this as a photoresist (UV), but it is also compatible with electron beams. It is spun on top of Py at 4000 rpm and baked at 110 °C for 1 min. The resulting

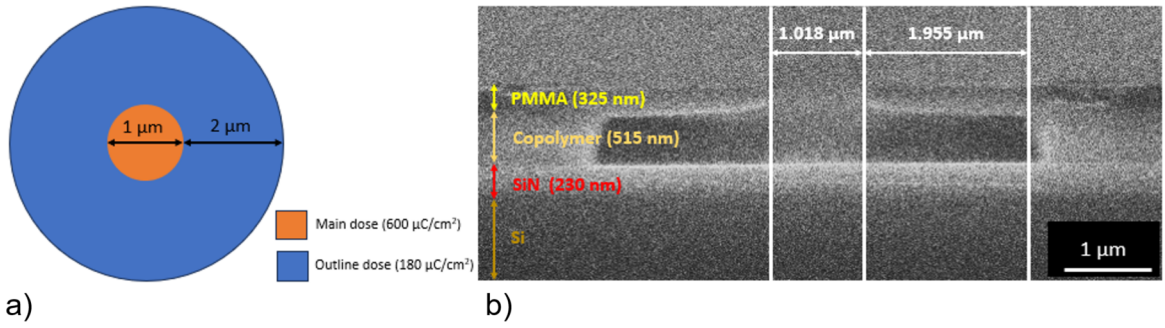

Figure 3: (a) Electron beam exposure scheme. (b) Cross section of developed resist with multi-dose exposure on a bulk substrate taken by SEM in snapshot mode.

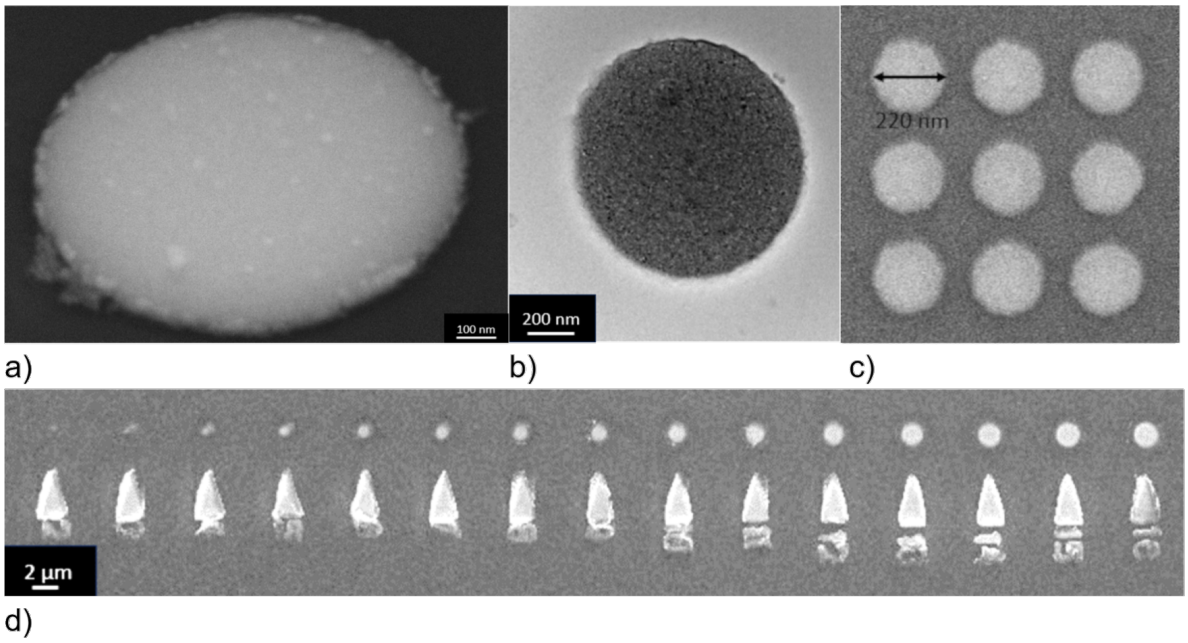

Figure 5: (a) SEM image of a Py disk (1 µm diameter, 50 nm thickness) at a tilt angle. (b) TEM image of a Py disk with 1 µm diameter. (c) SEM image of a 200 nm disk array with 50 nm spacing. (d) SEM image of Py nanodisks of different sizes.

thickness is around 448 nm for 1:1 diluted resist and around 203 nm for 1:2 diluted resist. The resist is exposed to 120 µC/cm^2 at 100 kV and then post-exposure baked at 110 °C for 2 min. The development is done by submerging the sample in AZ® 726MIF containing 2.38% tetramethylammonium hydroxide (TMAH) for 20 s.

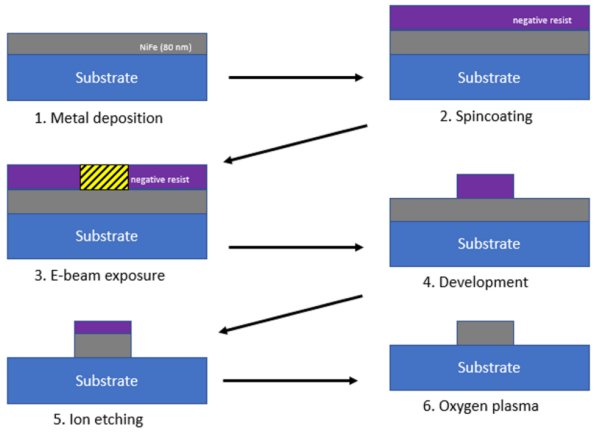

Figure 6: Ion beam etching process.

Once the resist is developed, IBE is performed. Since the ions diverge as they travel, the substrate is rotated to obtain a uniform ion flux on the substrate and a uniform etching rate between inner and outer sides. The highest etching rate can be achieved when the substrate is tilted at 45° since the etching rate of the primary beam is much bigger than the redeposition rate of etched materials. As observed in Figure 7, there was redeposition of etched material along the edge of the resist. This can be avoided by taking an additional step before etching the Py: The resist is heated at 120 °C for 5 min to reflow the resist and to create a meniscus shape, thus, decreasing the redeposition at the edge of the resist during etching.

The advantage of IBE are the well-defined structures with good edge sharpness (Figure 8). This technique offers high resolution for structures down to 200 nm, and dense structures with spacings as small as 50 nm can be created. Another advantage is the ability to deposit metal at high temperatures as the resist mask is applied after the metal deposition. However, there are also some drawbacks to consider. The sample is physically etched by argon bombardment, which results in a non-selective etching of the material. Non-selective etching means that not only Py is etched but also the resist and the SiN membrane. Areas around the nanodisks are thicker and rougher because of the lower etch rate near the structures and the redeposition of Py. In addition, the much thinner areas of the membrane away from the nanostructures can affect the overall mechanical stability of the membrane. Dry etching is generally better suited for bulk substrate applications as discussed in section “Preparation of nanostructures starting from a bulk substrate”.

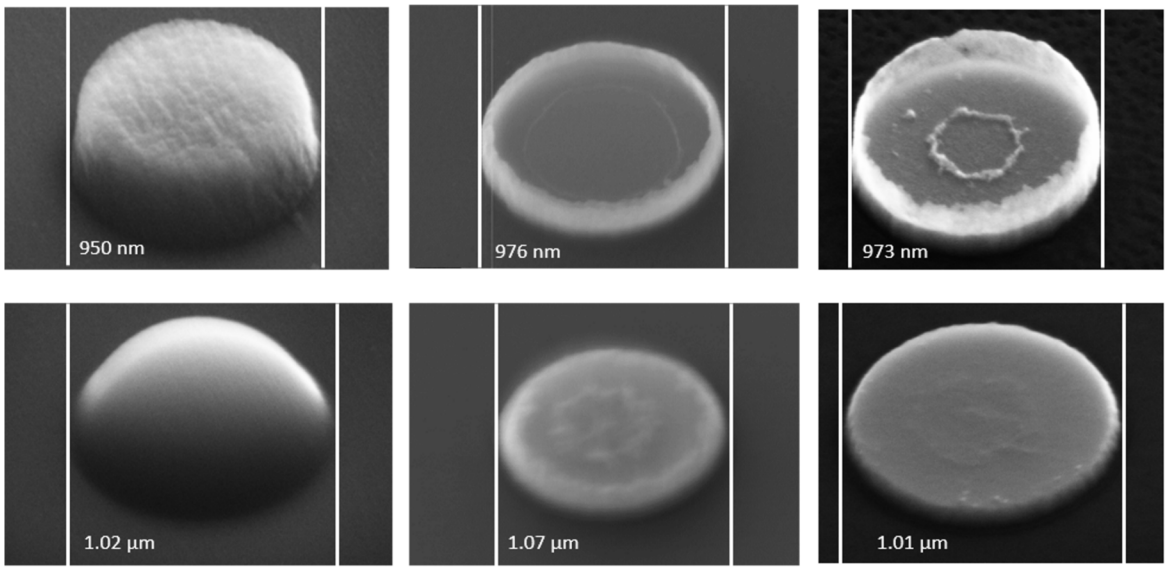

Figure 7: Comparison between normal patterned resist (top) and reflowed resist (bottom). From left to right: patterned resist, nanodisk after IBE, and nanodisk after plasma cleaning.

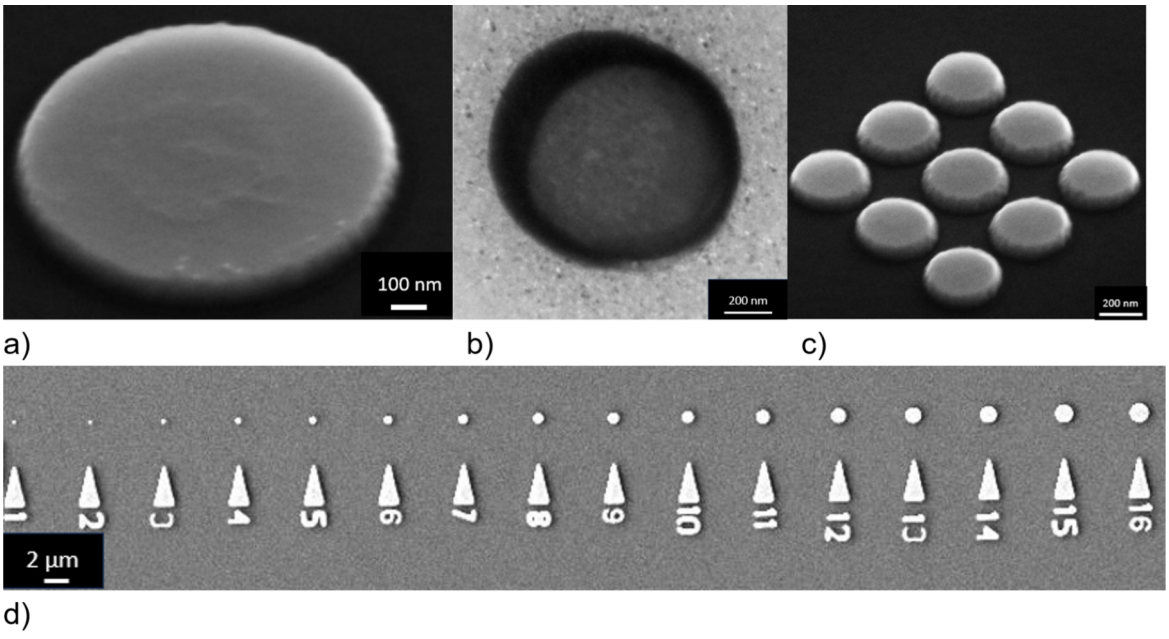

Figure 8: (a) SEM image of a Py disk (1 µm diameter, 80 nm thickness) at a tilt angle. (b) TEM image of a Py disk with 1 µm diameter. (c) SEM image of a 200 nm disk array with 50 nm spacing. (d) SEM images of nanodisk with different sizes.

Stencil lithography

Stencil lithography was implemented back in 1978 to fabricate thin-film Josephson devices [29]. The principle behind stencil lithography is to deposit materials onto the substrate through the aperture of a hard mask. Rather than placing the mask directly on the substrate and then removing it, as in traditional resist-based fabrication, stencil lithography employs a separate mask that is later aligned on the substrate and retains its aperture after the pattern transfer. This technique has advantages including simplicity in process, reusable masks, and the absence of resist masks. The latter eliminates common challenges associated with resist such as the edge bead problem and resist melting during deposition. This approach is ideal for applications on small substrates where spin coating of a homogeneous resist

layer is difficult. This technique is particularly suitable for TEM application because TEM grids have the SiN membrane that can be used as a hard mask.

The mask fabrication process (Figure 9a) is the following: A 200 nm thick sacrificial layer of aluminium was deposited by means of evaporation on a conventional TEM grid with a free-standing SiN membrane. The aluminium layer serves as a support for the free-standing membrane and as a conductive layer for better imaging during FIB milling. Then FIB milling was performed to create apertures in the SiN membrane representing the patterns to be transferred to the sample. Last, the aluminium layer was removed by submerging the mask in TMAH 3% solution. In this project, a TEM substrate with nine free-standing SiN membranes was used as a hard mask. We lay an identical substrate flat on the mask in a flip-chip configuration. The mask is aligned so that all nine windows are on top of each other, and the asymmetrically broken windows serve as an orientation aid. Substrate and mask were fixed using Kapton® foil with an adhesive layer. After deposition, the foil can be removed and the mask can be detached. The mask can still be used, but the resulting nanodots will be smaller than those obtained from the previous deposition because the aperture size on the mask is reduced by residual deposited material.

As seen in Figure 9c, the structure has a blurring effect. One of the sources of blurring in stencil lithography is the geometry of the source–stencil–substrate configuration. The deposited structure is larger than the stencil aperture. Their size difference (the blurring size) is proportional to the size of the source and the distance between the substrate and the mask, and inversely proportional to the sample-to-source distance [30]. It is then required to decrease the distance between the mask and the substrate as well as to employ an evaporation process from a distant point-like source. Furthermore, metal deposits on the mask aperture leads to clogging, causing masks to become ineffective after multiple uses.

Preparation of nanostructures starting from a bulk substrate

To avoid the delicate procedure of fabricating nanostructures on a free-standing SiN membrane, we initially fabricated the nanostructures on a 200 µm thick Si substrate with 100 nm thick SiN buffer layers on both sides. The buffer layers were deposited with low-pressure CVD to ensure stress-free films. The fabrication process is shown in Figure 10.

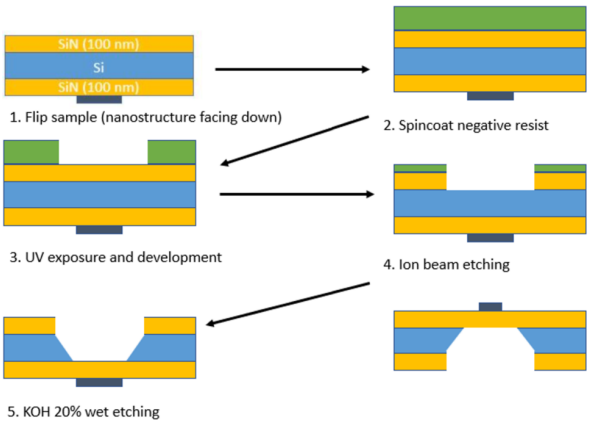

Figure 10: SiN membrane preparation on a nanostructure.

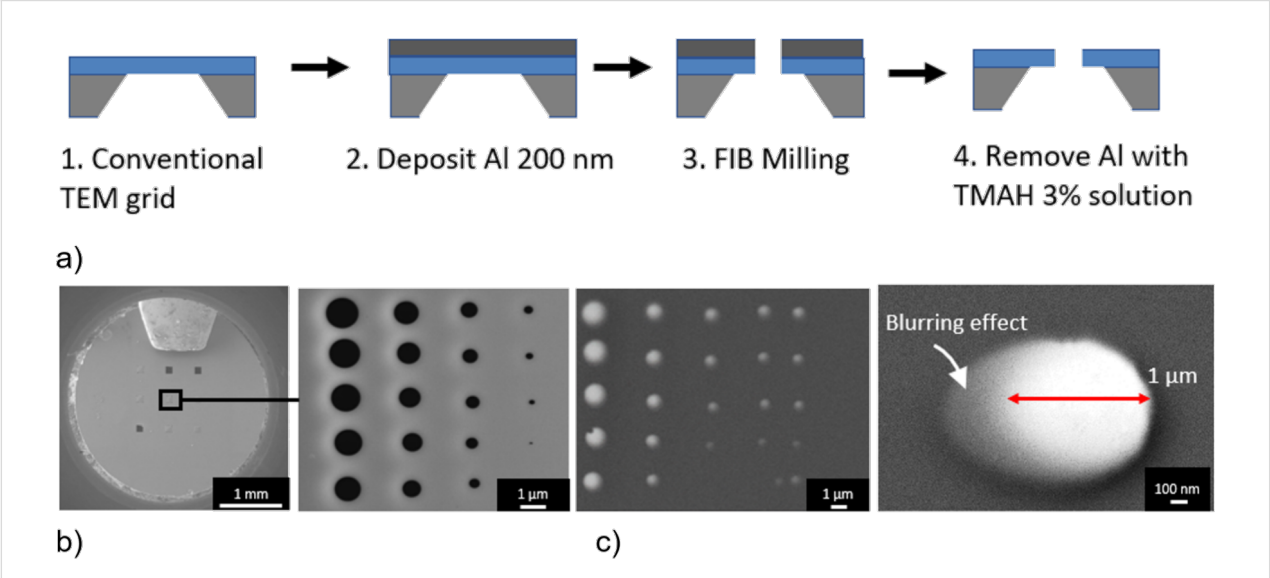

Figure 9: (a) Hard mask preparation. (b) SEM image of the hard mask. (c) SEM images of deposited Py and a 1 µm Py disk.

First, we made the nanostructure using lift-off or IBE methods on the bulk substrate. Then we protected the nanostructure with a resist and patterned AZ®5214E resist on the back side of the substrate using the image reversal technique. A window in the SiN buffer layer was prepared by ion beam etching through the aperture in the mask of AZ®5214E resist, and the remaining SiN layer served as a hard mask for the wet etching of the substrate's back side in 20% KOH solution. The KOH solution was heated to 60 °C to accelerate the process to an etching rate of approximately 9 µm/h in the direction perpendicular to the substrate surface. Using a warmer KOH solution resulted in a faster etch rate but led to much stronger bubbling and roughening of the Si surface with the creation of micropyramidal hillocks [31].

The surface alignment of the Si substrates is parallel to the {100} crystallographic plane of Si, and the anisotropic KOH etching results in a 54.7° slope with respect to the etched surface on the sidewalls. Because of the (010) edge orientation of Si substrates, etching occurs faster in diagonal directions of the substrates, resulting in sharp edges on the structure (Figure 11b).

Magnetic measurements

Setup

All TEM magnetic measurements were performed using an FEI Titan HOLO G2 60-300 microscope with an acceleration voltage of 300 kV with two biprisms. The microscope was used in the Lorentz mode, which gives a spatial resolution up to 2 nm. The sample was mounted on a standard double-tilt holder and inserted into the microscope. The magnetization of the sample was first saturated out-of-plane by switching on the objective lens of the TEM and then allowing it to relax. To switch the magnetic configuration, a small objective-lens field was applied, which resulted in in-plane (H_{ip}) and out-of-plane (H_{oop}) fields applied to the sample (Figure 12) depending on the sample tilt. We kept the tilt angle constant and applied different intensities of the objective-lens field. The magnetic states of the sample were characterized under each condition using LTEM and off-axis electron holography.

Lorentz TEM

The dynamics of the magnetic vortex with external magnetic field applied using the objective lens was first studied using

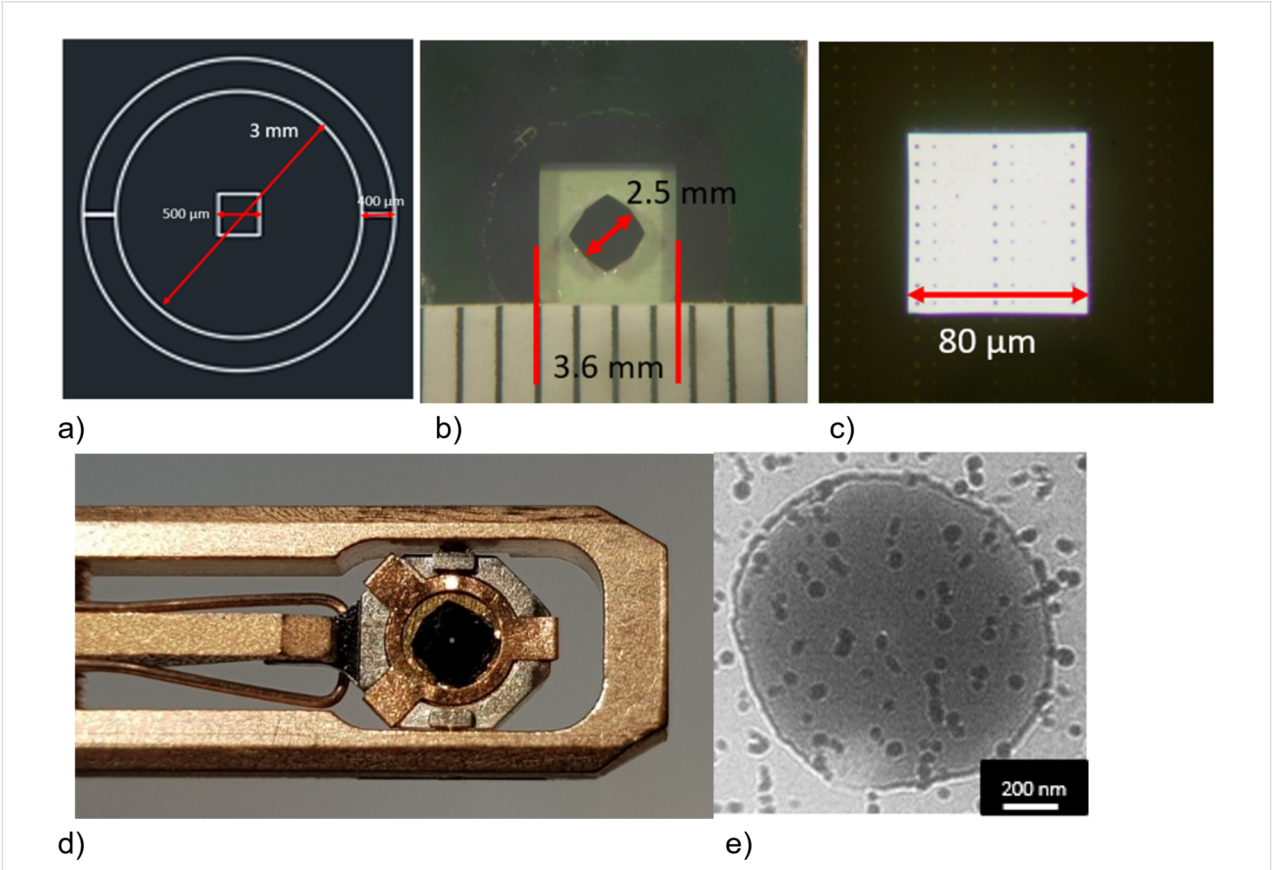

Figure 11: (a) Lithography mask. (b) Etched substrate still attached to the bulk substrate. (c) Free-standing SiN membrane. (d) The TEM substrate glued to a 3 mm ring is mounted on the TEM holder. (e) LTEM image of a 1 µm Py disk on a SiN membrane. The small dots are residuals of the protective resist layer.

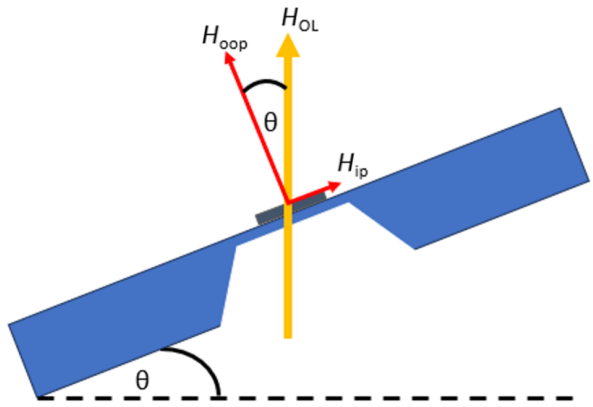

Figure 12: Tilted sample and the external magnetic field component.

Lorentz TEM. The initial magnetic configuration of the Py nanodisks after relaxation is shown in Figure 13c. In order to ascertain the coercive field of the sample, we applied the external field until the contrast was no longer visible, which means we saturated the magnetic components until all pointed to the same in-plane direction. The motion of the vortex with the field was studied using the following field sequence. First, we saturated the magnetic configuration by applying a large field. Then we decreased the external field until we observed the vortex followed by increasing the field in the opposite direction. In the end, we decreased the field to zero. LTEM images were captured at different magnetic fields along this sequence and are presented in Supporting Information File 1.

As the external magnetic field is applied, the vortex core (bright or dark spot) moves perpendicular to the applied field toward the edge of the disk such that the magnetization component aligned with the field grows bigger. The vortex core displacement near zero external field is in linear proportion to the applied magnetic field, which is consistent with prior results [32]. At the saturation field, the vortex core disappears because the magnetization is now in a single-domain state.

When the external magnetic field decreases, the formation of the vortex does not occur immediately, but after the field reaches about 30 mT (nucleation field), the bright spot appears near the edge of the disks. The same observation was made as we applied the opposite field direction until saturation and started decreasing it. The saturation field is larger than the nucleation field, which agrees with other works [7,8,33].

Off-axis electron holography

The limitations of LTEM are that (1) the magnetic contrast is visible only under defocused conditions, which significantly limits the spatial resolution, and that (2) magnetization information is not quantitative unless multiple LTEM images are taken at different focuses for further reconstruction using the transport of intensity equation. Using off-axis electron holography, we were able to directly measure the phase shift induced by the in-plane magnetization in focus and quantitatively. Using the same parameters as in the LTEM experiment, we kept the tilt angle of the sample constant and started with increasing the external field from 0 to 530 Oe (Figure 14 upper row), which is bigger than the saturation field we observed during the LTEM experiments. Then, we decreased the magnetic field back to 0 Oe (Figure 14 bottom row). We observed the movement of the vortex core with an applied objective-lens field. The vortex state started with counterclockwise helicity and moved perpendicular to the applied field. The magnetization before and after saturation was not similar under an external field of 335 Oe since nucleation started after the external field decreased to around 300 Oe. The results are consistent with the observations from LTEM.

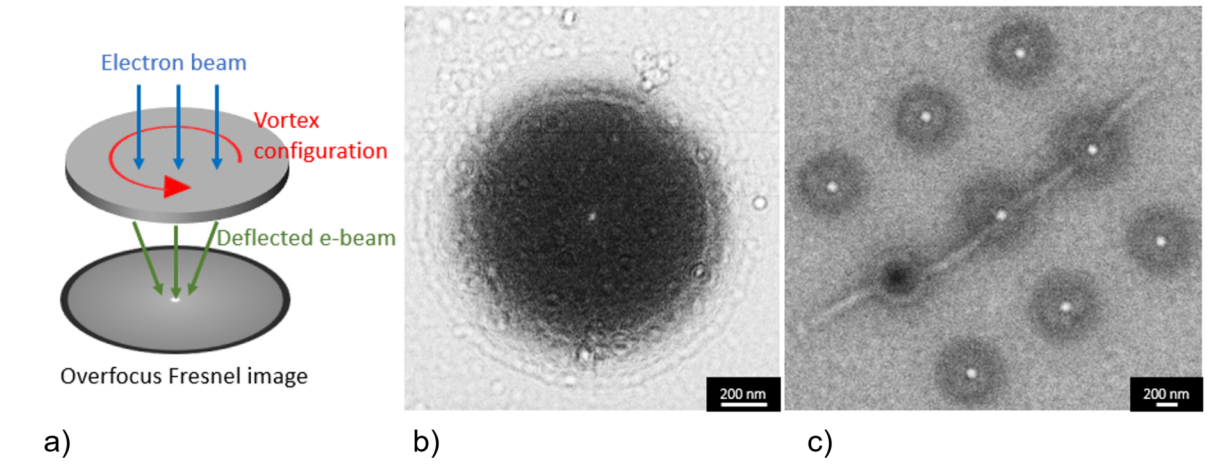

Figure 13: (a) Simplified illustration of the LTEM technique. (b) LTEM image of a 1 µm Py disk. (c) LTEM image of a 400 nm disk array.

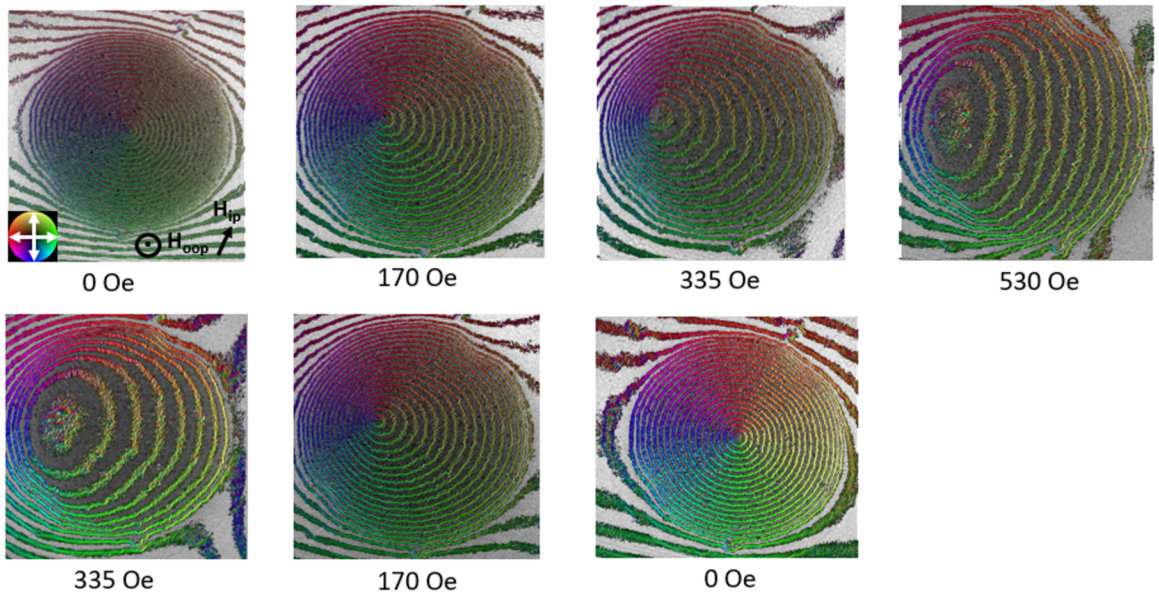

Figure 14: Magnetic induction map of a nanodisk under various magnetic fields obtained by off-axis electron holography. The fringes outside of the disk are probably caused by the charging of the SiN membrane.

Conclusion

Electron beam lithography in combination with lift-off and IBE methods for the preparation of Py nanodisks has been optimized. The results have been compared using SEM and TEM. In addition, the application of stencil lithography for the preparation of Py nanodisks has been demonstrated, and the results were compared with the results obtained with electron beam lithography.

Among these methods, dry etching stands out for its sharp and well-defined edges, while the hard mask method offers the least precise results. In a broader comparison, IBE outperforms the lift-off technique, delivering cleaner and more reproducible nanostructures with better spatial resolution. Lift-off fabrication allows for the creation of nanodisks with dimensions ranging from 400 nm to 1.6 µm, but as the size decreases, structural precision diminishes. In contrast, dry etching can yield nanodisks as small as 200 nm with high precision. However, it is important to consider that the IBE process may result in thinner SiN membranes, potentially compromising their mechanical stability. Furthermore, IBE, which is a physical etching process, redeposits a non-volatile metal layer on the resist, creating fences on the edge of the structure and contaminating the silicon nitride membrane. A possible solution is replacing IBE with reactive ion etching (RIE). Using RIE, there would be less redeposition since the reaction between gas and etched metal will form a gaseous compound or volatile particles, which can be pumped out. RIE of nickel–iron alloys has been carried out using inductively coupled plasma RIE with argon and chlorine [34] or with NH_3 and CO [35]. Stencil lithography requires further optimization although possible applications are attractive because of the flexibility of the patterns, reusable masks, and resistless fabrication. This would be useful because TEM grids are too small for standard lithography. After all, spin-coated resist on TEM grids has inhomogeneous thickness because of edge beads, which become too large relative to the diameter of the TEM grid. Alignment of the stencil mask in a flip-chip configuration with the sample under clean room conditions prior to metal deposition plays an important role as a single dust particle can increase the gap between the mask and the sample up to about 100-fold, thereby increasing the shadowing effect greatly.

KOH etching opens further applications for TEM sample preparation for more complicated high-resolution nanostructures. We have developed a straightforward method to prepare a SiN membrane with nanostructures on one side. This method allows for the use of an ultrasonic bath, higher deposition temperatures, and a homogeneous resist layer, all of which are difficult to obtain with free-standing SiN membranes, resulting in more reproducible results. In principle, some characterizations that do not require an electron-beam-transparent membrane can be done while the nanostructures are on a bulk substrate. Once all measurements have been completed, KOH etching can be conducted, and as a result, the sample is placed on a free-standing SiN membrane and can be studied under TEM. This is useful for future high-frequency correlative characterization of multilayer spintronic devices. Another possible further development

is to use a different membrane, for example SiC (lattice constant a = 0.435 nm), since it can grow as a single-crystalline layer and ensure epitaxial sample growth on top of it, for example, the growth of NbN (a = 0.439 nm) with a lattice mismatch of 1%. Epitaxial growth of Py films on single-crystal SiC membranes is also feasible. Py epitaxial films were obtained on single-crystal MgO substrates [36] that have a lattice constant of 0.42 nm. It was demonstrated that the epitaxial SiC layer can serve as an excellent mask material for KOH etching of Si [37]. However, etching to a crystalline membrane might be different from etching to a free-standing amorphous SiN membrane. The structural integrity of a free-standing crystalline membrane during KOH etching is still to be investigated. An alternative to KOH etching would be FIB milling [38] or RIE [39].

Supporting Information

Supporting Information File 1

Video of Lorentz TEM measurements.
[https://www.beilstein-journals.org/bjnano/content/supplementary/2190-4286-15-1-S1.mp4]

Acknowledgements

The authors gratefully acknowledge the possibility of performing parts of the work at ER-C-1, HNF, PGI-4/JCNS-2, PGI-5, and PGI-7 in Forschungszentrum Jülich GmbH. The authors also thank R. Borowski, L. Kibkalo, L. Risters, S. Neduev, M. Nonn, H. Stumpf, S. Trellenkamp, F. Lentz, E. Neumann, O. Petracic, S. Nandi, B. Schmitz and G. Potemkin for technical assistance.

Funding

This research was funded in parts by the EU Horizon 2020 Research and Innovation Programme (Grant No. 856538, project “3D MAGiC”) and the Joint Laboratory on Model and Data Driven Material Characterization of the Helmholtz Association.

ORCID® iDs

Joshua Williams - https://orcid.org/0009-0004-5414-8753
Michael I. Faley - https://orcid.org/0000-0003-2768-2796
Rafal E. Dunin-Borkowski - https://orcid.org/0000-0001-8082-0647

References

1. Raabe, J.; Pulwey, R.; Sattler, R.; Schweinböck, T.; Zweck, J.; Weiss, D. *J. Appl. Phys.* **2000,** *88,* 4437–4439. doi:10.1063/1.1289216
2. Shinjo, T.; Okuno, T.; Hassdorf, R.; Shigeto, K.; Ono, T. *Science* **2000,** *289,* 930–932. doi:10.1126/science.289.5481.930
3. Pulwey, R.; Rahm, M.; Biberger, J.; Weiss, D. *IEEE Trans. Magn.* **2001,** *37,* 2076–2078. doi:10.1109/20.951058
4. Liu, Y.; Gliga, S.; Hertel, R.; Schneider, C. M. *Appl. Phys. Lett.* **2007,** *91,* 112501. doi:10.1063/1.2780107
5. Pang, Z.; Yin, F.; Fang, S.; Zheng, W.; Han, S. *J. Magn. Magn. Mater.* **2012,** *324,* 884–888. doi:10.1016/j.jmmm.2011.10.012
6. Xu, M.; Jiang, G.; Zhang, Z.; Li, R.; Meng, D.; Zhang, J. *J. Phys. D: Appl. Phys.* **2022,** *55,* 325303. doi:10.1088/1361-6463/ac6d8b
7. Okuno, T.; Shigeto, K.; Ono, T.; Mibu, K.; Shinjo, T. *J. Magn. Magn. Mater.* **2002,** *240,* 1–6. doi:10.1016/s0304-8853(01)00708-9
8. Schneider, M.; Hoffmann, H.; Zweck, J. *Appl. Phys. Lett.* **2000,** *77,* 2909–2911. doi:10.1063/1.1320465
9. Harvey, T. R.; Rubiano da Silva, N.; Gaida, J. H.; Möller, M.; Feist, A.; Schäfer, S.; Ropers, C. *MRS Bull.* **2021,** *46,* 711–719. doi:10.1557/s43577-021-00166-5
10. Weßels, T.; Däster, S.; Murooka, Y.; Zingsem, B.; Migunov, V.; Kruth, M.; Finizio, S.; Lu, P.-H.; Kovács, A.; Oelsner, A.; Müller-Caspary, K.; Acremann, Y.; Dunin-Borkowski, R. E. *Ultramicroscopy* **2022,** *233,* 113392. doi:10.1016/j.ultramic.2021.113392
11. Fu, X.; Pollard, S. D.; Chen, B.; Yoo, B.-K.; Yang, H.; Zhu, Y. *Sci. Adv.* **2018,** *4,* eaat3077. doi:10.1126/sciadv.aat3077
12. Vansteenkiste, A.; De Baerdemaeker, J.; Chou, K. W.; Stoll, H.; Curcic, M.; Tyliszczak, T.; Woltersdorf, G.; Back, C. H.; Schütz, G.; Van Waeyenberge, B. *Phys. Rev. B* **2008,** *77,* 144420. doi:10.1103/physrevb.77.144420
13. Kammerer, M.; Stoll, H.; Noske, M.; Sproll, M.; Weigand, M.; Illg, C.; Woltersdorf, G.; Fähnle, M.; Back, C.; Schütz, G. *Phys. Rev. B* **2012,** *86,* 134426. doi:10.1103/physrevb.86.134426
14. Dieterle, G.; Gangwar, A.; Gräfe, J.; Noske, M.; Förster, J.; Woltersdorf, G.; Stoll, H.; Back, C. H.; Schütz, G. *Appl. Phys. Lett.* **2016,** *108,* 022401. doi:10.1063/1.4939709
15. Mehrnia, M.; Trimble, J.; Heinonen, O.; Berezovsky, J. *Phys. Rev. Appl.* **2021,** *16,* 034049. doi:10.1103/physrevapplied.16.034049
16. Cowburn, R. P. *J. Magn. Magn. Mater.* **2002,** *242–245,* 505–511. doi:10.1016/s0304-8853(01)01086-1
17. Lloyd, J. C.; Smith, R. S. *J. Appl. Phys.* **1959,** *30,* S274–S275. doi:10.1063/1.2185927
18. McKeehan, L. W.; Cioffi, P. P. *Phys. Rev.* **1926,** *28,* 146–157. doi:10.1103/physrev.28.146
19. Arnold, H. D.; Elmen, G. W. *J. Franklin Inst.* **1923,** *195,* 621–632. doi:10.1016/s0016-0032(23)90114-6
20. Dhankhar, M.; Vaňatka, M.; Urbanek, M. *J. Visualized Exp.* **2018,** No. 137, e57817. doi:10.3791/57817
21. Faley, M. I.; Williams, J.; Lu, P.; Dunin-Borkowski, R. E. *Electronics (Basel, Switz.)* **2023,** *12,* 2144. doi:10.3390/electronics12092144
22. Bryan, M. T.; Atkinson, D.; Cowburn, R. P. *J. Phys.: Conf. Ser.* **2005,** *17,* 40–44. doi:10.1088/1742-6596/17/1/006
23. Reeve, R. M.; Elmers, H.-J.; Büttner, F.; Kläui, M. Magnetic Imaging and Microscopy. In *Handbook of Magnetism and Magnetic Materials;* Coey, M.; Parkin, S., Eds.; Springer International Publishing: Cham, Switzerland, 2021; pp 1–52. doi:10.1007/978-3-030-63101-7_28-1
24. Kovács, A.; Dunin-Borkowski, R. E. Magnetic Imaging of Nanostructures Using Off-Axis Electron Holography. In *Handbook of Magnetic Materials;* Brück, E., Ed.; Elsevier: Amsterdam, Netherlands, 2018; pp 59–153. doi:10.1016/bs.hmm.2018.09.001

25. Allresist. Positive E-Beam Resists AR-P 610 series. https://www.allresist.com/wp-content/uploads/sites/2/2020/03/AR-P610_english_Allresist_product-information.pdf (accessed Aug 24, 2023).
26. Edelstein, A. S. *Nanomaterials: Synthesis, Properties and Applications;* Inst. of Physics Publ.: Bristol, U.K., 2001.
27. Dolan, G. J. *Appl. Phys. Lett.* **1977,** *31,* 337–339. doi:10.1063/1.89690
28. Bogdanov, A. L.; Andersson, E. K. Fine undercut control in bilayer PMMA-P(MMA-MAA) resist system for e-beam lithography with submicrometer resolution. In *Electron-Beam, X-Ray, and Ion-Beam Submicrometer Lithographies for Manufacturing, Proc. SPIE 1465,* Microlithography, San Jose, CA, USA, Aug 1, 1991; SPIE: Bellingham WA, USA, 1991. doi:10.1117/12.47368
29. Dunkleberger, L. N. *J. Vac. Sci. Technol. (N. Y., NY, U. S.)* **1978,** *15,* 88–90. doi:10.1116/1.569443
30. Vazquez-Mena, O.; Villanueva, L. G.; Savu, V.; Sidler, K.; Langlet, P.; Brugger, J. *Nanotechnology* **2009,** *20,* 415303. doi:10.1088/0957-4484/20/41/415303
31. Schröder, H.; Obermeier, E.; Steckenborn, A. *J. Micromech. Microeng.* **1999,** *9,* 139–145. doi:10.1088/0960-1317/9/2/309
32. Uhlig, T.; Rahm, M.; Dietrich, C.; Höllinger, R.; Heumann, M.; Weiss, D.; Zweck, J. *Phys. Rev. Lett.* **2005,** *95,* 237205. doi:10.1103/physrevlett.95.237205
33. Guslienko, K. Y.; Novosad, V.; Otani, Y.; Shima, H.; Fukamichi, K. *Phys. Rev. B* **2001,** *65,* 024414. doi:10.1103/physrevb.65.024414
34. Park, H. J.; Ra, H.-W.; Song, K. S.; Hahn, Y.-B. *Korean J. Chem. Eng.* **2004,** *21,* 1235–1239. doi:10.1007/bf02719500
35. Kim, S. D.; Lee, J. J.; Lim, S. H.; Kim, H. J. *Nippon Oyo Jiki Gakkaishi* **1999,** *23,* 252–254. doi:10.3379/jmsjmag.23.252
36. Ohtake, M.; Tanaka, T.; Matsubara, K.; Kirino, F.; Futamoto, M. *J. Phys.: Conf. Ser.* **2011,** *303,* 012015. doi:10.1088/1742-6596/303/1/012015
37. Mohd Nasir, N. F.; Shah, C. M.; Leech, P. W.; Reeves, G. K.; Pirogova, E.; Istivan, T.; Tanner, P.; Holland, A. S. Fabrication of 3C-Silicon Carbide Membranes: Towards Development of Novel Microdevices for Biomedical Applications. In *2012 International Conference on Biomedical Engineering (ICoBE),* Penang, Malaysia, Feb 27–28, 2012; IEEE, 2012. doi:10.1109/icobe.2012.6178985
38. Mayr, S.; Finizio, S.; Reuteler, J.; Stutz, S.; Dubs, C.; Weigand, M.; Hrabec, A.; Raabe, J.; Wintz, S. *Crystals* **2021,** *11,* 546. doi:10.3390/cryst11050546
39. Faley, M. I.; Bikulov, T. I.; Bosboom, V.; Golubov, A. A.; Dunin-Borkowski, R. E. *Supercond. Sci. Technol.* **2021,** *34,* 035014. doi:10.1088/1361-6668/abda5c

License and Terms